Novel application of Ru-based catalysts on MgAl oxides alkaline adsorbents for cyclic CO2 methanation

Chemical Engineering Journal 501 (2024) 157585

Contents lists available at ScienceDirect

Chemical Engineering Journal

journal homepage: www.elsevier.com/locate/cej

Novel application of Ru-based catalysts on MgAl oxides alkaline adsorbents for cyclic CO_2 methanation

Andrea Rizzetto, Enrico Sartoretti, Marco Piumetti *, Raffaele Pirone, Samir Bensaid

Department of Applied Science and Technology (DISAT), Politecnico di Torino Corso Duca degli Abruzzi 24, 10129 Turin, Italy

ARTICLE INFO

Keywords:
Ru catalysts
MgAl-based supports
Dual Function Materials
CO_2 hydrogenation
Cyclic methanation

ABSTRACT

This study explores the performances of Ru-based catalysts with a low metal content (2 wt%) supported on MgO and Mg-Al Oxides (MgAl) for cyclic CO_2 adsorption and methanation at atmospheric pressure. Adsorption and desorption tests demonstrated that MgAl-based catalysts are more promising for CO_2 capture due to their larger surface area and better distribution of active sites (Mg^{2+}–O^{2-}). Moreover, doping the MgAl support with K_2CO_3 further improves surface alkalinity and, consequently, capture performance. During cyclic operations, all the catalysts proved effective and selective for methane production. To simulate realistic conditions, both dry and wet CO_2 adsorptions were conducted before the methanation stage. The presence of moisture positively influenced gas carbonation for all catalysts, increasing the overall amount of CO_2 captured. Specifically, Ru/MgAl exhibited the best performance in terms of adsorption and conversion to methane (approximately 85 % after dry adsorption and 79 % after wet adsorption), with a maximum methane production of 183 and 220 $\mu mol_{CH4}\ g^{-1}$, respectively. The reaction yield was further enhanced with Ru-K/MgAl, achieving 327 $\mu mol_{CH4}\ g^{-1}$ after dry adsorption and 333 $\mu mol_{CH4}\ g^{-1}$ after wet adsorption. However, this catalyst displays different conversion kinetics, attributed to slowed carbonate migration, low Ru dispersion, limited specific surface area, and excessive carbonation strength. *Operando* FTIR tests revealed differences in reaction intermediates between Ru/MgAl and Ru-K/MgAl, by going deeper into the kinetic differences observed. The study concludes that Ru/MgAl materials are highly promising catalysts for CO_2 adsorption and methane production, supporting the development of technologies for CO_2 abatement and renewable energy utilisation.

1. Introduction

Human activities like industrial agriculture, intensive farming, fish farming, and deforestation are exceeding the planet's regenerative capacity. Fossil fuel use and industrial infrastructure are significantly increasing greenhouse gas emissions, driving climate change. It is therefore essential to adopt sustainable habits and reduce the use of fossil fuels to reverse environmental degradation and pollution. Developing efficient and sustainable energy solutions is crucial [1–4]. Currently, electricity production from renewable energy sources (RES) is growing rapidly, helping to reduce carbon dioxide emissions and reliance on fossil fuels [5].

This transition entails the emergence of new challenges, including, for example, intermittent power generation from renewable sources (e.g., wind, solar, hydroelectric…), along with new solutions related to power grid management and energy storage [6–8]. New catalytic technologies to produce synthetic natural gas or liquid fuels (e.g., hydrocarbons or alcohols) [9–12] from CO_2 can be the solution to the simultaneous management of both carbon emission mitigation and storage of renewable energy in excess. Therefore, an interesting way to develop long-term, high-capacity electricity storage may lie in power-to-gas (PtG) systems [13–17]. In this configuration, 'green' hydrogen is produced by electrolysis of water using excess electricity from renewable sources. The H_2 produced then reacts with carbon dioxide through the Sabatier reaction, generating methane (Eq. (1):

$$CO_2 + 4H_2 \rightarrow CH_4 + 2H_2O \Delta H_{298K,1bar} = -165.0\,kJ/mol \quad (1)$$

The synthetic methane produced in this way can be directly injected into the existing natural gas network, always in compliance with pipeline requirements [16].

In today's economy, methane plays a key role as an energy carrier in industry, electricity production, and transport, thanks to its widespread distribution infrastructure. Currently, most of the consumed methane

* Corresponding author.
E-mail address: marco.piumetti@polito.it (M. Piumetti).

https://doi.org/10.1016/j.cej.2024.157585
Received 5 August 2024; Received in revised form 24 October 2024; Accepted 9 November 2024
Available online 10 November 2024

comes from fossil natural gas resources. However, synthetic methane produced from renewable energy sources and recycled CO_2 in PtG plants represents a promising alternative, which could contribute to the decarbonisation of all those sectors heavily dependent on fossil gas. With this in mind, many sources of carbon can be considered, from CO_2 released by fossil-fuel power plants and other carbon-intensive industries to atmospheric CO_2 [18].

Typically, nickel-based catalysts are used to conduct methanation reactions at up to 30 bar pressures with an inlet temperature of around 250/300 °C [19]. In addition, significant kinetic limitations characterise the complete hydrogenation of carbon dioxide, a reaction involving eight electrons, although methanation is thermodynamically favoured ($\Delta G_{298K} = -130.8$ kJ mol^{-1}) [20,21]. Thus, the presence of a catalyst is crucial to have high selectivity and conversion rates. Therefore, a fundamental role in the energy transition is played by the research and development of a suitable catalyst to achieve adequate activity, selectivity and stability values, while also taking economic issues into account [14,21]. However, Ni is prone to deactivation in the presence of sulphur compounds, moisture, and oxygen. Consequently, Ni-based catalysts could significantly lose their conversion capability in the case of a real CO_2 stream, as exhaust fumes, and in continuous adsorption and hydrogenation cycles [22]. Therefore, Ru-based systems may be considered more suitable when designing an ideal catalyst for PtG applications [23–25]. Conversely to the traditional direct CO_2 methanation, a cyclic process could enhance the operational and energy efficiency of the process. This configuration allows the reduction of system costs and complexity by more effectively utilising the heat generated from the exothermic reaction to facilitate CO_2 desorption. In addition to contributing to decreasing CO_2 emissions, this process can be effectively coupled with discontinuous renewable hydrogen sources for sustainable methane production [26].

Among the numerous adsorbents examined in the literature, magnesium oxide (MgO) is a promising candidate for CO_2 capture due to its surface basicity and ability to generate oxygen vacancies, enhancing CO_2 adsorption [27,28]. Compared to other metal oxide adsorbents, such as those based on lithium and calcium, MgO offers the advantage of a lower regeneration temperature (< 500 °C) [28]. It is particularly effective in intermediate temperature ranges (200–400 °C) and has a high theoretical CO_2 uptake capacity of 24.8 mmol/g [29]. CO_2 adsorption on MgO occurs through the interaction of acidic CO_2 molecules with the basic O^{2-}–Mg^{2+} sites, forming several types of carbonate species [28]. However, pure MgO faces challenges despite its potential, including low surface area, slow adsorption kinetics, and thermal stability issues during high-temperature desorption, which may lead to sintering and reduced efficiency [30]. In this context, Mg-based hydrotalcite (HT) materials (also known as layered double hydroxides, LDHs) have gained increasing attention as CO_2 adsorbents and precursors for catalysts for methanation reaction, as it is possible to obtain materials with large metal surface area, small metal particle size, excellent thermal stability and uniform distribution of active sites [31,32]. Layered double hydroxides are inorganic crystalline materials composed of divalent and trivalent metal ions characterised by interesting features: adsorption speed, easy regeneration, and good thermal stability [33]. These alkaline adsorbents can react with CO_2 over a wide temperature range. Alkali metal impregnation, especially with potassium, is a common technique for enhancing material alkalinity [34,35]. Many articles indicate that a typical potassium loading of 20 wt% [36–38] is optimal for achieving the highest equilibrium sorption capacity. Moreover, contrary to other reactions [39–42], these materials demonstrate remarkable capabilities even in the presence of moisture, as the mechanism proceeds through the formation of transient hydroxylated species that in turn react with CO_2 to form carbonates. According to previous reports, the kinetics of CO_2 adsorption on these hydroxylated compounds is faster than that on pure metal oxides, promoting the CO_2 capture process [33,43].

In contrast to the well-studied HT-supported Ni catalysts, the application of Ru-based hydrotalcite-derived materials for CO_2 adsorption and methanation cycles is still scarce, to the best of the authors' knowledge. The first application of these systems to CO_2 reduction can be found in the work of Xu et al. [44] in which Ru-based MgAl-HT derived catalysts were prepared, characterised, and tested for non-thermal plasma (NTP) activated CO_2 hydrogenation. The latter work evidenced that, under the NTP conditions, the ruthenium-based catalyst enabled significantly high CO_2 conversion and CH_4 yield at relatively low temperatures; in addition, treatment conditions remarkably affected the chemical state of the metal and metal-support interaction, thus altering the activity of the catalysts. More recently, Misol et al. [45] studied MgAl-HT-based Ru-derived catalysts with different Ru loadings and promoted them with La^{3+} for direct CO_2 methanation experiments. They observed, however, that the catalysts showed low activity in the low-temperature range and poor selectivity towards CH_4. The addition of La^{3+}, while contributing to the basicity, had no significant effect on performance.

Based on these premises, the present work explores the use of Ru-based catalysts supported on MgO and Mg-Al-based oxides (MgAl) for cyclic CO_2 adsorption (under both dry and wet conditions) and methanation at atmospheric pressure. The catalysts were prepared using wetness impregnation with an aqueous solution of the ruthenium precursor. Catalytic experiments were conducted in a laboratory setup designed for the selected application, utilising 5 vol% CO_2 in N_2 and 5 vol% H_2 in N_2. The study thoroughly examined different aspects, including the role of the surface alkalinity, the influence of moisture (10 % humidity in the feed gas), and the effect of doping on CO_2 chemisorption and subsequent activation, employing various characterisation techniques, including XRD, nitrogen physisorption at −196 °C, CO_2-TPD, H_2-TPR, FESEM, EDX, ICP-MS, and *operando* FTIR spectroscopy.

2. Experimental

2.1. Preparation of MgO and Mg-Al-based supports

A high surface area MgO support was synthesised via template-assisted hydrothermal methodology, inspired by Gao et al. [43].

MgAl-based materials were prepared through calcination at 400 °C for 5 h (heating ramp 2 °C min^{-1}) of a synthetic hydrotalcite produced by Sigma Aldrich with a Mg/Al ratio fixed at 3 (condensed formula $Mg_6Al_2(CO_3)(OH)_{16}{\cdot}4H_2O$). In the manuscript, the term 'MgAl' will refer to the calcined form of synthetic hydrotalcite, which corresponds to an amorphous combination of Mg and Al oxide layers in which the MgO is excellently dispersed.

MgAl-doped with K_2CO_3 (K/MgAl) was synthesised via incipient wetness impregnation: in details, 1.8 g of MgAl was impregnated with 3 mL Milli-Q water solution of 0.36 g of K_2CO_3, corresponding to 20 % of carbonate (Sigma Aldrich, ≥99.0 %). Subsequently, the powder was left to dry at 120 °C for 16 h and calcined at 400 °C for 4 h with a 2 °C min^{-1} heating ramp.

2.2. Preparation of Ru-based catalysts

Ru-based catalysts were prepared by employing a water solution of ruthenium (III) nitrosyl nitrate (1.5 % w/w Ru − Sigma Aldrich) to impregnate MgO, MgAl, and K/MgAl samples dropwise. These materials were dried at 120 °C overnight, calcined at 400 °C for 4 h in air, and finally reduced with 5 vol% H_2 in N_2 at 400 °C for 1 h. The nominal Ru loading was 2 wt% for all the samples.

2.3. Characterisation and experimental procedures

A Thermo Scientific iCAP RQ ICP-MS device was employed to perform the elemental analysis of Ru-based catalysts. 20 mg of powder catalysts were dissolved in a solution of phosphoric acid, hydrofluoric acid, and sulfuric acid (4 mL: 2 mL: 4 mL) and the slurry was heated at

220 °C for 15 min (rate 10 °C min^{-1}) in a microwave digestor. Afterwards, proper metal concentration solutions were prepared by diluting the parent digestate solutions.

Crystallographic analysis was carried out by means of an X Pert PANalytical diffractometer equipped with a radiation source given by Cu anode (Kα = 1.5418 Å) and a PiX accelerator detector. Powder samples were placed on a flat zero background sample holder and diffraction patterns were collected from 10° to 80° (2θ) with a Bragg-Brentano geometry (voltage 40 kV; current 40 mA). The identification of the crystalline phases was performed thanks to HighScore Plus® software and Scherrer's equation was used to calculate the mean crystallite size of the phases after the instrumental peak broadening correction with LaB_6 standard diffractogram.

Nitrogen physisorption at −196 °C was performed through a Micromeritics ASAP TRISTAR 3020 instrument. Before the analysis, the catalyst surface was cleaned by possible adsorbed components thanks to a thermal pretreatment that occurred at 400 °C for 2 h in a specifically dedicated system (Micromeritics FlowPrep 060). Brunauer-Emmett-Teller (BET) method was applied in the relative pressure range from 0.05 to 0.3 in order to estimate the specific surface area (S_{BET}) of the catalyst; furthermore, the Barrett-Joyner-Halenda (BJH) algorithm was employed for the desorption branch to calculate the pore volume and pore average size.

A Zeiss Merlin with a Gemini-II column and an Oxford x-act X-ray detector allowed to perform the morphological analysis. Micro- and nanographs were collected with a backscattered electron detector (AsB − *Angle selective Backscattered*) to better highlight the presence and the dispersion of ruthenium spots on oxide supports. Moreover, elemental analysis and a further investigation of elemental distribution were carried out through FESEM-EDX mapping. A 5 nm thick layer of platinum was deposited via sputter coating on the sample powder, before the analysis.

The surface basicity of the as-prepared catalyst was evaluated through CO_2 temperature programmed desorption (CO_2-TPD) performed in a laboratory set-up consisting of a reactor with a fixed adsorbent bed, a furnace, and a gas analyser. Desorption profiles were collected with dedicated adsorption–desorption experiments in dry and wet conditions (10 vol% of H_2O in addition to the flow) in order to study the strength of supports and catalysts' basic sites in different reaction settings. In a typical experiment, ca. 400 mg of catalyst were pelletised, crushed, and sieved (300–212 μm), loaded into a U-shaped reactor, and pretreated at 400 °C for 2 h in N_2 flow (heating ramp 5 °C min^{-1}). Then, the temperature was lowered to 250 °C (the set point chosen for the methanation experiments) and a 5 vol% flow of CO_2 in N_2 was sent to the catalyst for 30 min. Thereafter, the system was purged with N_2 keeping the temperature constant. The desorption step was performed by heating the sample from 250 °C to 500 °C with a 5 °C min^{-1} ramp under a stream of N_2. The limit temperature of 500 °C was selected to prevent thermal decomposition of the catalysts [38]. The total gas flow rate was fixed at 90 mL min^{-1} for the entire experiment. In the case of Ru-functionalised catalysts, a reductive step with 5 vol% of H_2 in N_2 was performed during the thermal pretreatment in order to remove additional carbonyl species on the surface.

Temperature-programmed reduction (H_2-TPR) analyses were carried out with the same laboratory setup. Circa 100 mg of non-reduced catalyst powder was prepared and activated following the same procedure described for CO_2-TPD analysis, but without any reductive step. Then, after cooling down to 50 °C, a gas flow of 50 mL min^{-1} containing 5 vol% H_2 in N_2 was sent to the reactor, and the temperature was ramped up to 400 °C with a heating ramp of 5 °C min^{-1}.

Adsorption and methanation tests were performed in the same laboratory set-up adopted for the temperature-programmed techniques. All the catalysts were prepared following the procedure described above. The CO_2 adsorption stage was performed in dry and wet conditions (10 vol% of H_2O in addition to the flow) at constant temperature (250 or 320 °C), flowing 5 vol% of CO_2 in N_2. After purging CO_2 with pure N_2 for ca. 30 min, a gas mixture of 5 vol% of H_2 in N_2 was sent to the materials for at least 30 min at the same temperature (250 or 320 °C). A scheme of the experimental operations is depicted in Fig. 1. The set-up was equipped with an EMERSON X-STREAM XE gas analyser, provided with the following channels: a nondispersive infrared detector for CO, CO_2, and CH_4, a thermal conductivity detector for H_2, and a paramagnetic sensor for O_2. In each adsorption step, the amount of adsorbed CO_2 was calculated using the following equation (Eq. (2)):

$$q_{CO_2 adsorbed}\left(\mu molg^{-1}\right) = \frac{\dot{Q}_{in}\frac{P}{RT}\int_{t_0+\Delta t}^{t_f}\left(\frac{y_{CO_{2,in}}-y_{CO_{2,out}}}{1-y_{CO_{2,out}}}\right)dt}{m_{catalyst}} \quad (2)$$

where $\dot{Q}_{in}$ is the total inlet flow rate, $y_{CO_{2,in}}$ represents the mole fraction of CO_2 in the inlet recorded by gas analyser at the beginning of each experiment, $y_{CO_{2,out}}$ is the mole fraction of the CO_2 in the outlet, $\Delta t(s)$ is the assumed delay time of gas analyser measurement, and m is the weight of the catalyst. The pressure considered is 1 atm and the temperature is that of gas flowing through mass flow controllers, namely 25 °C. As regards the quantification of the methane produced, it was carried out through Eq. (3):

$$\widehat{n}_{CH_4,prod}\left(\mu molg^{-1}\right) = \frac{\dot{Q}_{in}\frac{P}{RT}\int_{t_0+\Delta t}^{t_f}\left(\frac{y_{CH_{4,out}}}{1+y_{CH_{4,out}}}\right)dt}{m_{sorbent}} \quad (3)$$

where $\dot{Q}_{in}$ is the total inlet flow rate, $y_{CH4,out}$ is the mole fraction of the CH_4 in the outlet, $\Delta t(s)$ is the assumed delay time of gas analyser measurement, and m is the weight of the catalyst. The yield of the reaction was estimated through Eq. (4).

$$Y_{CH_4}(\%) = \frac{\mu mol_{CH_{4\,out}}}{\mu mol_{CO2,ads} - \mu mol_{CO2,des}} \times 100 \quad (4)$$

Time-resolved *operando* Fourier Transform Infrared spectroscopy (FTIR) was conducted using a Bruker Invenio S® spectrometer with an MCT detector. The spectra of the catalysts were obtained in transmittance mode, covering the range from 4000 to 800 cm^{-1} with a spectral resolution of 2 cm^{-1}. The samples were compressed at 2 tons to produce thin tablets [46,47]. The samples were placed in a Specac® high temperature and high-pressure cell (HTHP cell) equipped with ZnSe windows. The same protocol used for the catalytic tests (Fig. 1) was applied for the spectroscopy analysis of the catalyst surface. All the spectra were normalised with respect to the density of the tablets. The gas mixtures were sent to the catalyst using mass flow controllers, and the cell outlet was connected to the same analysers utilised during the catalytic tests (*vide supra*). For clarity, it should be mentioned that all spectra were baseline-corrected relative to that of the activated surface.

3. Results and discussion

3.1. Structural and morphological properties

The elemental composition of Ru/MgO, Ru/MgAl and Ru-K/MgAl catalysts was investigated by the ICP-MS technique; EDX was also employed, scanning for the weight percentages of Mg, Al, K and O atoms. The results of ICP analysis for Ru and EDX spectroscopy for K are shown in Table 1. The experimental percentage is slightly lower due to a possible metal loss during the synthesis or dilution procedures in the case of Ru/MgO. Upon comparing the Ru/MgAl and Ru-K/MgAl samples, characterisation by ICP-MS reveals that impregnation with Ru occurred in the desired manner, with an actual Ru percentage close to 1.95 wt%. As far as EDX results are concerned, the detection of K amount is in line with the theoretical expectation. Similar conclusions were found for Mg, Al and O.

The diffraction profiles obtained for the as-prepared catalysts were

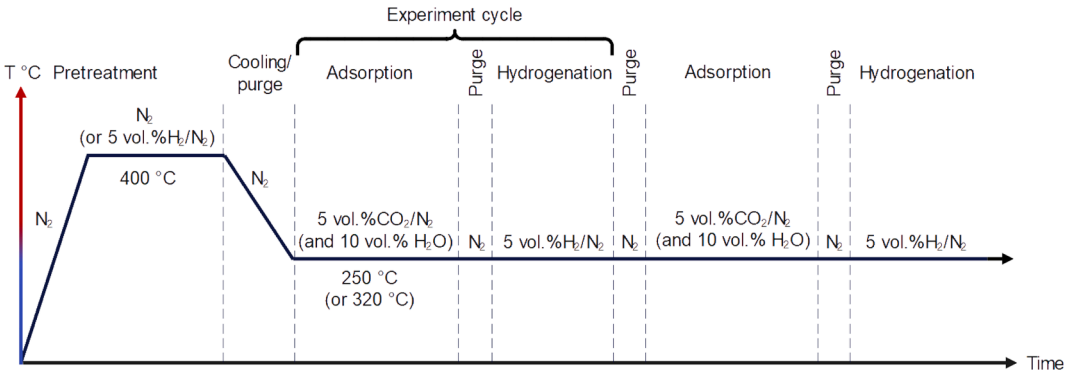

Fig. 1. Cyclic methanation experiment profile.

Table 1
Summary of elemental analyses of Ru/MgO, Ru/MgAl, and Ru-K/MgAl catalysts by ICP-MS for Ru and EDX for K.

Sample	Nominal Ru wt. %	Nominal K wt. %	Ru wt. % [a]	K wt. % [b]
Ru/MgO	1.95	––	1.50	––
Ru/MgAl	1.95	––	1.95	––
Ru-K/ MgAl	1.95	9.3	2.01	8.5

(a) Inductively coupled plasma Mass Spectrometry (ICP-MS).
(b) Energy dispersive X-ray spectroscopy (EDX).

compared with the ICDD PDF-2 Release 2004 database, which is shown for comparison in Fig. 2. The high surface area MgO support possesses the classical face-centred cubic (FCC) crystalline phase of MgO, called periclase. Characteristic MgO peaks at 2θ angle values of 36.9° (111), 42.9° (200), 62.2° (220), 74.6° (311), and 78.5° (222) are clearly recognisable. The enlarged shape and low signal intensity indicate a smaller number of atoms within the crystals capable of constructively interacting with the X-ray beam. This is directly dependent on a low degree of crystallinity and on the small size of the crystallites. These assumptions were validated by applying Scherrer's equation, which returns an average crystallite size of about 8 nm.

Ru/MgO shows the characteristic peaks of MgO illustrated before. Ru

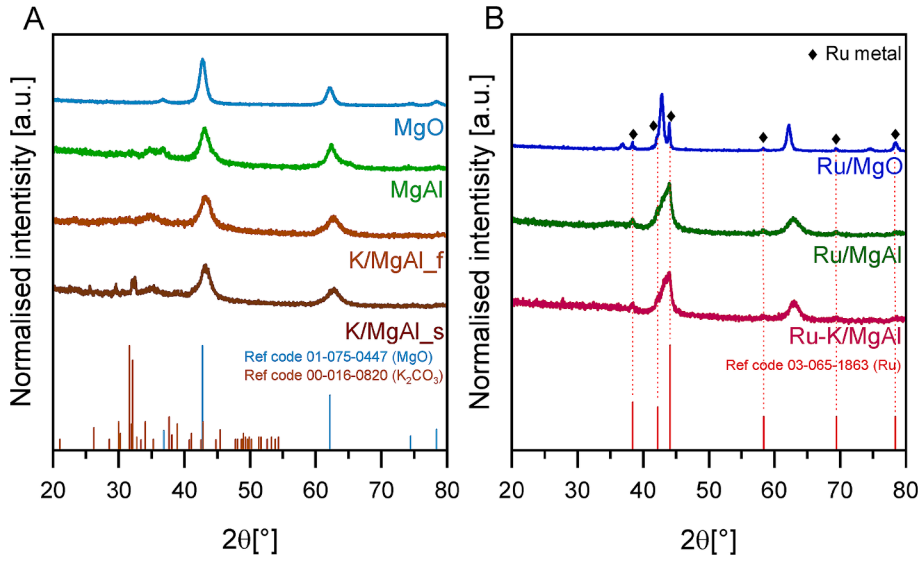

Fig. 2. XRD patterns of A) supports and B) Ru-functionalised catalysts with their respective reference codes.

Table 2
Summary of structural properties from XRD analysis and physisorption of N_2.

Sample	D [nm] [a]	S_{BET} [m^2 g^{-1}] [b]	Pore Volume [cm^3 g^{-1}] [c]	Average Pore Width [nm] [c]
MgO	8 (MgO)	131	0.164	5
Ru/MgO	37 (Ru)16 (MgO)	57	0.286	16
Pristine LDH	–	8	0.017	13
MgAl	4 (MgO)	223	0.150	5
Ru/MgAl	9 (Ru)4 (MgO)	218	0.219	6
K/MgAl	4 (MgO)	47	0.060	6
Ru-K/MgAl	16 (Ru)5 (MgO)	27	0.084	14

(a) XRD analysis;
(b) Calculated according to Brunauer-Emmett-Teller (BET) method;
(c) Calculated according to the Barrett-Joyner-Halenda (BJH) algorithm.

is recognisable due to the main peaks at angles 2θ of 38.4° (100), 42.2° (002), 44.0° (101), 58.3° (102), 69.4° (110) and 78.4° (103) typical of the compact hexagonal packing (hcp) of the metal. The average size of Ru crystallites was 37 nm and that of MgO crystallites was 16.3 nm (Table 2). As also confirmed by other analysis techniques, the impregnation of Ru was detrimental to the MgO support, which lost some morphological characteristics during the production of the final catalyst. Furthermore, much of the metal appears to be arranged in medium to large aggregates (see FESEM description). As mentioned in *section 2.2*, the catalyst was treated at high temperatures and in a reducing atmosphere. However, considering the high Hüttig temperature of Ru (over 500 °C) [48], it was assumed that the low dispersion may stem from the synthesis method and the poor metal-support interaction between Ru and MgO. The interaction between Ru and MgO itself is also dictated by the synthesis methodology and/or the type of chemical precursors employed.

Considering the MgAl-based catalysts, all diffractograms show the presence of the MgO (periclase) phase with a face-centred cubic crystal structure with characteristic peaks at 2θ angle values of 37.1° (111), 43.1 (200), 62.5° (220), 75.0° (311), 78.9° (222). MgAl clearly presents the MgO crystalline phase, but at slightly different values of angle 2θ, with intensity reduced to half that of pure MgO and with more spiky peaks. These observations respond to a smaller unitary crystal structure and to the presence of a more amorphous and finely dispersed MgO phase in the material. The shift of the peaks at different angles probably indicates interaction and partial substitution of Al^{3+} ions in the Mg^{2+} ion structure, which identifies a good degree of material defectiveness [38]. The average size of the MgO crystallites within the MgAl structure was found to be about 4 nm. This value is indicative of a considerable dispersion of the MgO phase, a characteristic that increases the ability to adsorb CO_2 [49,50]. The Al_2O_3 phase, on the other hand, is not particularly visible within the diffractograms. This could be attributed to the low level of crystallinity of alumina, which is almost only present in the amorphous phase, and to a certain degree of interaction between aluminium and magnesium ions to form spinel structures such as $MgAl_2O_4$ [51].

In the case of the K/MgAl sorbent, the characteristic peaks of the MgO phase remained recognisable, but the intensities further decreased. This could be due to a partial collapse of the MgAl structure upon doping [52]. Looking at the range between 20° and 45°, the presence of potassium carbonate seems to have greatly influenced the final diffractogram of the material. However, the peaks are not defined, and this could suggest a good incorporation of the carbonate phase on the MgAl together with a large dispersion of the K_2CO_3 crystallites. Even analysing the spent K/MgAl sorbent (Fig. 2**A**, K/MgAl_s), the XRD confirmed the presence of potassium carbonate with more defined peaks than the fresh synthesised material (Fig. 2**A**, K/MgAl_f). This difference could be attributed to slight rearrangement and aggregation of the K_2CO_3 crystallites to form more recognisable particles. For Ru/MgAl and Ru-K/MgAl (Fig. 2**B**), although the signals are quite noisy, metallic Ru is visible at angles 2θ of 38.4° (100), 42.2° (002), 44.0° (101), 58.3° (102), 69.4° (110) and 78.4° (103).

As described above, all diffractograms show the presence of the periclase phase with changed intensities and peak shapes. Ru/MgAl exhibits MgO crystallites characterised by an average size of 4 nm; therefore, it could be assumed that the impregnation did not change or worsen the structure of the double oxide. In addition, the size of the Ru crystallites has an average value of around 9 nm (Table 2), which prefigures a good dispersion of the metal, although a true distribution of their size is not available. As far as Ru-K/MgAl is concerned, the

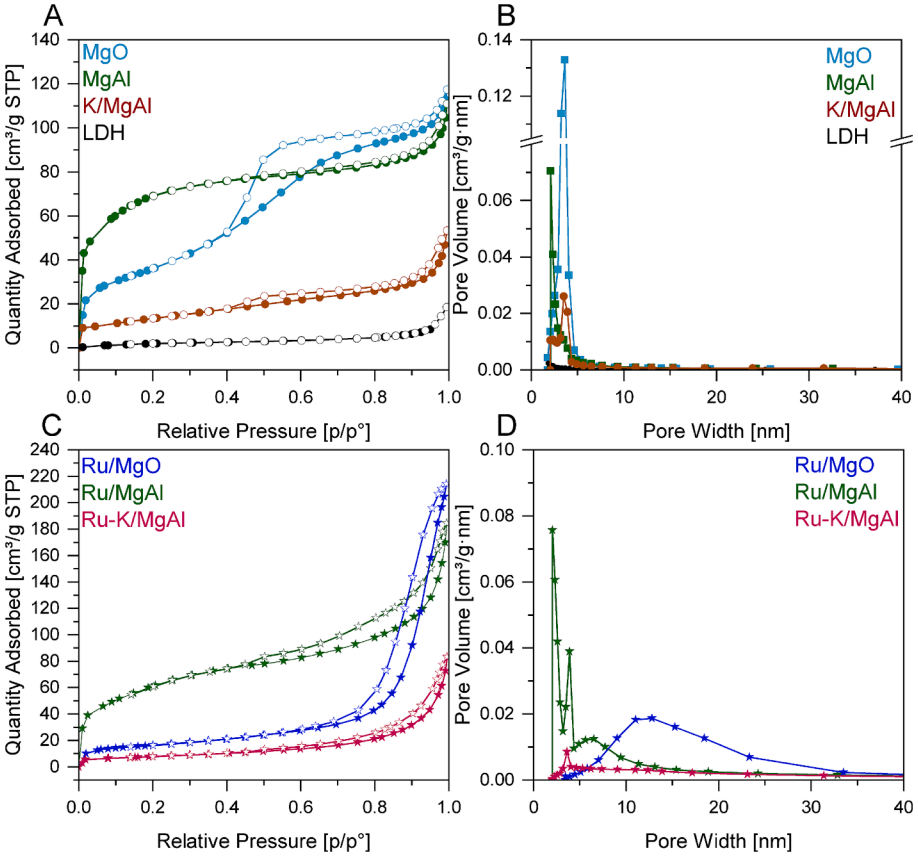

Fig. 3. Physisorption analysis of N_2 at −196 °C. A) Isotherms of the MgO, MgAl, K/MgAl, and pristine LDH supports and B) porosity distributions obtained by BJH method for the support materials C) Isotherms of the Ru/MgO, Ru/MgAl, and Ru-K/MgAl catalysts and D) porosity distributions obtained by BJH method for the Ru-functionalised catalysts.

presence of K_2CO_3 could be recognised in the first part of the diffractogram but is hardly visible. Unlike MgAl and K/MgAl, Ru-K/MgAl has slightly larger MgO crystallites, as well as Ru crystallites with an average size of 15.9 nm. This could result from difficulties encountered during impregnation in wetness mode.

The results of nitrogen physisorption at −196 °C for the various supports and catalysts are depicted in Fig. 3 through the isotherms obtained from the amount of nitrogen physisorbed (Fig. 3**A-C**) and pore size distribution (Fig. 3**B** — **D**). The numerical values of specific surface area, pore volume and average pore size obtained with the BET and BJH models are shown in Table 2. The shape of the isotherms of the samples was analysed following the IUPAC designation [53]. The MgO support has a high surface area of 131 m^2g^{-1}. This value is directly dependent on the hydrothermal synthesis technique, which guarantees the generation of a high number of defects and thus of alkaline active sites on the surface and theoretically capable of adequately dispersing any metal nanoparticles [54]. It is characterised by a type IV isotherm, which is classic for mesoporous materials with an H4-type hysteresis cycle, indicating the presence of microporosity [55]. The pores of MgO have a single-mode distribution centred around 4 nm. The functionalisation procedure seems to have distorted the morphology of the substrate, which lost a large part of its surface area (almost 57 %) from 131 to 57 m^2g^{-1}; in addition, an increase in pore volume and an unusual formation of large-sized porosity (around 16 nm) was observed.

Concerning MgAl supports, all samples possess adsorption isotherms of type IV, which are typical of mesoporous materials according to the IUPAC designation. Furthermore, all materials do not appear to have adsorption limitations at high relative pressures, and thus the hysteresis cycles may all belong to the H3 type, i.e., related to flat slab-like particles and slit-like pores [56]. Typically, uncalcined hydrotalcite possesses a low surface area and small pore volume with a little hysteresis loop due to nanoscale porosity around 13 nm in diameter. Once calcined, hydrotalcite assumes the structure of MgAl (also known in the literature by the acronym LDO, Layered Double Oxides [38]) and gains a surface area of 223 $m^2\ g^{-1}$ and a pore volume of 0.15 $cm^3\ g^{-1}$. The average pore size decreases to 5 nm, with a distribution centred on this

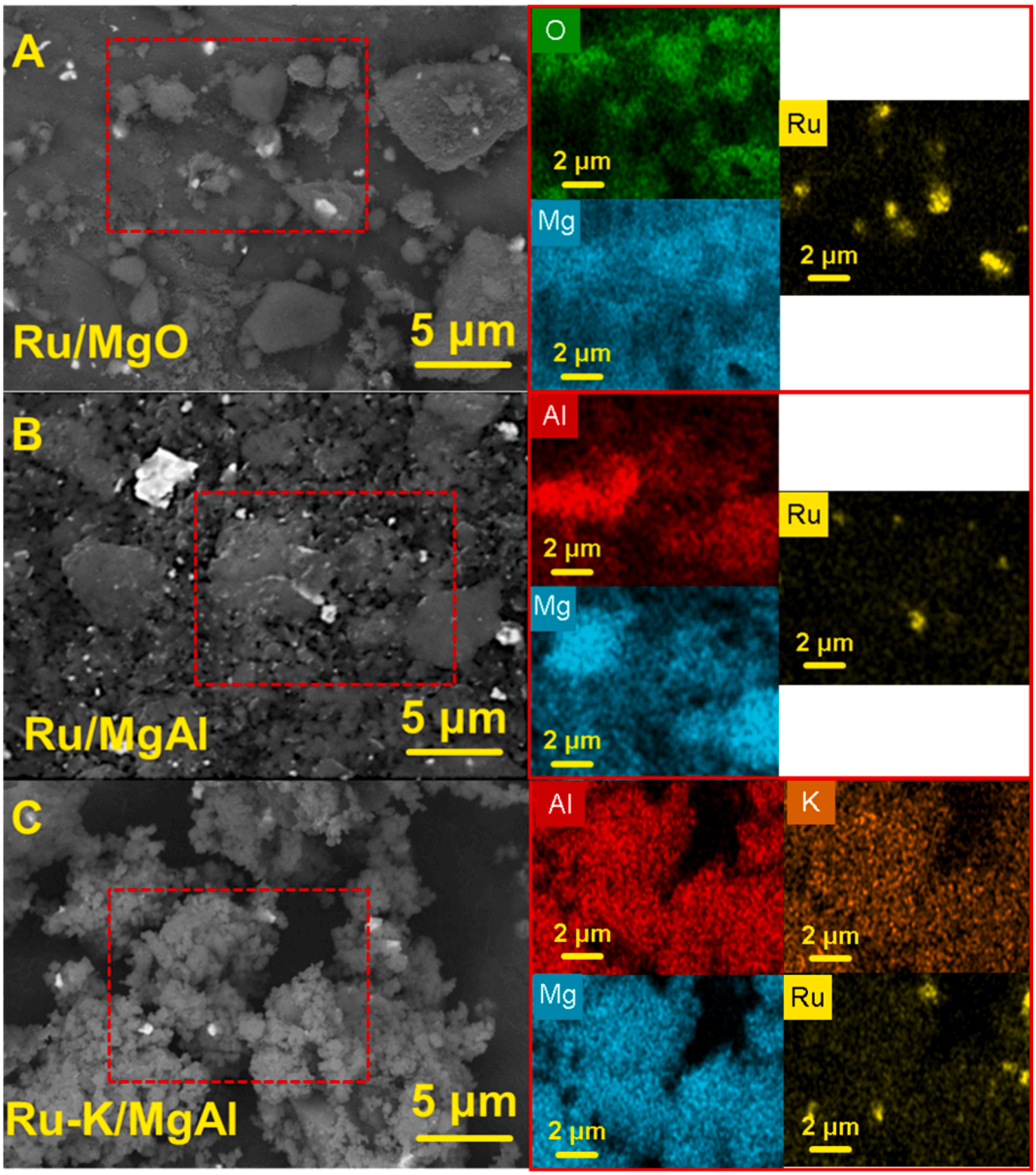

Fig. 4. FESEM images of A) Ru/MgO, B) Ru/MgAl, and C) Ru-K/MgAl catalysts, collected in backscattering mode, and associated EDX maps revealing element distribution.

value. These data underlined the importance of the first heat treatment, which is able to determine the final structure of the MgAl support. This occurs because dehydration, dehydroxylation of the layers, as well as decarbonation of the interlayer charge-compensating carbonate anions progressively occurs during the heat treatment. These phenomena generate a rearranged mixed-oxide final structure where the Mg species are dispersed in an amorphous Al matrix with a high surface area [57–59]. Impregnation with Ru nitrosyl nitrate on the MgAl sorbent, as already concluded with the crystallographic analysis, appears to occur without major changes in the substrate and only with a slight decrease in specific surface area to 218 $m^2\ g^{-1}$. Ru/MgAl also seems to possess a slightly increased average pore size. The pore size distribution remains mostly centred on 4.5 nm, with a tailing up to 30 nm. This could be imputable to the structural modification effect of the porosity by the precursor during impregnation. Doping with 20 wt% of K_2CO_3 on the MgAl substrate lowered the specific surface area value by up to 47 $m^2\ g^{-1}$ through a significant porosity occlusion effect. Indeed, the pore volume is reduced to 0.06 $cm^3\ g^{-1}$, but the pore size distribution does not change [38,60]. Subsequent impregnation with Ru of the K/MgAl material has the same effect as observed above, i.e., decreases surface area and increases pore volume and pore size, probably due to an occlusion of some porosity by the precursor. The lower surface area and porosity characterise Ru-K/MgAl. As will be discussed later, these textural characteristics, together with the microscopic information, mainly influenced the reaction rate to methane rather than CO_2 adsorption, as the presence of potassium carbonate has the advantage of increasing surface basicity and defects [50].

FESEM micrographs of Ru-based catalysts were acquired at varying magnifications on the micrometre and nanometer scale and through a secondary electron detector (InLens) and/or a backscattered electron detector (AsB – Angle selective Backscattered) to highlight the presence of metal particles on the surface. MgO support is characterised by a peculiar structure composed of thin petal-like plates, from which a vast internal porosity is articulated (**Figure S1** in the *Supporting information file*). Considering Ru/MgO, the images acquired and reported in Fig. 4**A** clarify the changes that occurred during catalyst synthesis, already pointed out by XRD and nitrogen physisorption analyses. The structure of the sample appears considerably different compared to that of the pristine support, and this may clarify the considerable loss of specific surface area discussed above. The impregnation may have been aggressive towards the MgO mesoporosity, significantly changing the morphology. The bright spots in Fig. 4 correspond to large metal clusters of 200–300 nm formed on the slightly jagged surface of the substrate, as also confirmed by EDX maps [61]. In line with other characterisations, this indicates low dispersion and possible weak interaction between Ru and MgO. Ru/MgAl (Fig. 4**B**) appears to possess a highly defective surface area, characterised by smaller and more disordered globular structures. Additionally, there is a notable dispersion of the metal, likely attributed to the increased surface area of the support. Regarding Ru-K/MgAl (Fig. 4**C**), the image reconstructed from backscattered electron signals reveals the globular structure of the material. EDX maps distinctly highlight the good dispersion of potassium, which seems to homogeneously cover the entire surface. As observed in the N_2 physisorption analysis, doping with K_2CO_3 has blocked a significant portion of the MgAl porosity, thereby significantly reducing the specific surface area of the final catalyst. The presence of large metallic agglomerates indicates poor dispersion of Ru on the Ru-K/MgAl catalyst.

3.2. Temperature programmed analyses

To better understand the type of basic Mg^{2+}–O^{2-} sites characteristic of sorbents and to get an idea of their CO_2 adsorption capacity, several CO_2-TPD analyses were conducted directly in the plant and from the temperature at which the material was then tested for cyclic methanation, namely 250 °C. According to the literature, the broadened profiles of the desorption curves can be caused by the release of CO_2 bound to sites of different bond strengths: between 200 and 300 °C, bidentate carbonate type species ($MgCO_3$) with medium basicity are desorbed; higher temperatures (> 300 °C) are required to release monodentate carbonates from extremely alkaline sites with high bond strength [43]. CO_2 adsorption tests with 10 % H_2O and desorption were conducted to observe the effect of moisture during carbonate formation on the basic sites of the support. It is well known that in the case of alkaline oxide-based adsorbents, the presence of water can increase the performance of MgO in terms of both kinetics and effective capacity [43,62,63]. Indeed, the oxide reacts preferentially with water to form intermediates in the form of $MgO{\cdot}H_2O$ and $Mg(OH)_2$, which are more reactive than the oxide. Diffusion is also intensified, since these intermediates possess a higher molar volume and cause the pores to enlarge, allowing CO_2 to move more easily [63].

As regards the Ru/MgO catalyst, the "dry" TPD profile (Fig. 5**A**, blue line) discloses a main asymmetric desorption peak centred at 316 °C, with a tail towards high temperatures. Therefore, Ru/MgO is mainly characterised by medium-strength basic sites. CO_2 adsorption in the presence of moisture (light blue line) does not change the desorption profile but intensifies the amount of CO_2 adsorbed and desorbed in the same temperature range, as expected. Actually, the amount of CO_2 desorbed increased from 117 μmol/g (145 μmol/g of CO_2 adsorbed) in the dry case to 148 μmol/g in the wet experiment (189 μmol/g adsorbed).

Thanks to the calcination stage, the LDH structure undergoes structural changes which allow it to obtain an amorphous phase with a high grade of defectivity. Gao et al. [64] studied this transformation coupling the results of XRD and ^{27}Al solid NMR analysis. The thermal treatment involves a migration of Al^{3+} cations from the MgO lattice to the surface. This migration generates new Mg-O active sites through two possible mechanisms: one involves the formation of defective sites through the substitution of Al^{3+} species for Mg^{2+} species in the periclase MgO lattice. Because of the difference in ionic radii and charge between the two cations, the structure gets distorted and the adjacent oxygen anions become coordinatively unsaturated. Another mechanism can involve the diffusion of a portion of inserted Al^{3+} out of the octahedral sites. Therefore, these sites are left vacant, and this new condition consequently produces three active Mg-O species around it. The enhanced defectivity together with the high surface area allows MgAl-based materials to achieve better adsorption performance than Ru/MgO, as demonstrated by TPD curves. In the dry experiment, Ru/MgAl (Fig. 5**B**, dark green line) adsorbed 301 μmol/g and released ca. 167 μmol/g of CO_2; compared to the Ru/MgO TPD profile, the peak shifts to 328 °C and the tail to higher temperatures appears more intense, suggesting the presence of higher basic strength sites on the support surface. Even in this case, the presence of moisture enhances the performance of the material, which adsorbed 357 μmol/g and released ca. 208 μmol/g. Conversely to Ru/MgO, the increase in desorbed CO_2 was also accompanied by a shift in the position of the peak, which is centred at 337 °C (light green line). This behaviour could be attributable to the nature of the active sites on which carbonates are formed. It is conceivable that the increase in material capacity that takes place in the presence of water is precisely due to the activation of normally unexploited active sites that are probably present on surface areas of low defect, i.e., terraces. On the other hand, according to Fagerlund et al. [65], the presence of moisture creates a surface layer of increased dissolution of Mg^{2+} species and consequently a larger layer of $MgCO_3$. The shift of the desorption peak to higher temperatures is therefore caused by a thicker carbonate layer that is more difficult to desorb, also due to diffusive limitations. By doping the MgAl support with K_2CO_3, the adsorbing capacity is significantly enhanced through the generation of more stable carbonates at higher temperatures (Fig. 5**C**), despite the loss in surface area. Ru-K/MgAl was able to adsorb ca 429 μmol/g in *dry* conditions and to release approximately 222 μmol/g. In the *Supporting information file,* an image comparing the intensity scales of the CO_2 TPD profiles is provided (**Figure S2**). Several studies [36,50,66,67] testified that K_2CO_3

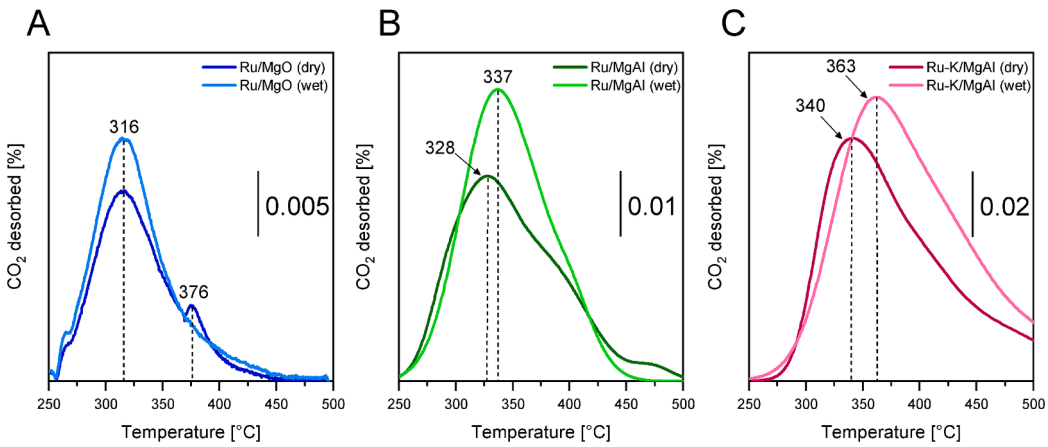

Fig. 5. CO_2-TPD profiles of A) Ru/MgO, B) Ru/MgAl, and C) Ru-K/MgAl catalysts obtained after dry and wet adsorption tests.

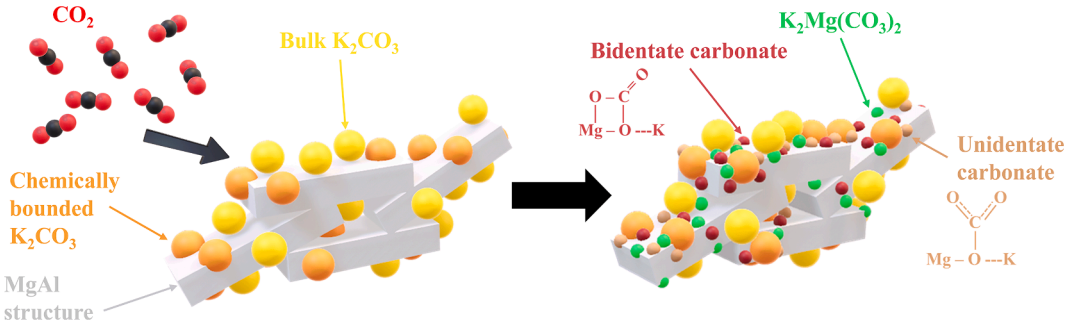

Scheme 1. Schematic representation of the formation of carbonate species on the MgAl surface promoted by K_2CO_3 doping. Figure adapted from Zhu et al [38].

on the surface participates in CO_2 adsorption by forming double K-Mg and $MgCO_3$ carbonates ($K_2Mg(CO_3)_2$) with high thermodynamic stability (higher operating temperatures) [68,69]. In addition, doping K_2CO_3 increases CO_2 adsorption capacity through surface modification. Moreover, Zhu et al. [38] hypothesised that K^+ ions react with unsaturated oxygen on the surface, forming K-O-Mg sites with increased reaction activity. Surface modification dominates especially those MgAl supports with a low Mg/Al ratio (as in this paper), probably due to increased unsaturated oxygen sites created by Al^{3+} substitution. A schematic depiction of the possible routes for CO_2 adsorption of K/MgAl is reported below (Scheme 1).

Therefore, this new synergy between alkali metal dopant and support dictates the further operating condition for the catalytic application of this material. In the *wet* experiment, the Ru-K/MgAl catalyst captured 558 μmol/g and desorbed 299 μmol/g with the subsequent heat treatment. The remarkable role of K_2CO_3 was also validated in the case of CO_2 absorption in the presence of moisture. In their works, Coenen et al. [70,71] investigated the mechanism for CO_2 and H_2O adsorption on a potassium-promoted hydrotalcite. They individuated that mainly K_2CO_3 interactions with Al centres would be responsible for activating reactive CO_2 adsorption sites, which can only be regenerated with steam. Moreover, they confirmed the existence of a further adsorption site for CO_2, which was activated in the case of a simultaneous supply of CO_2 and moisture to the catalyst. This outcome could further substantiate increasing the effectiveness of these materials in wet conditions. Quantitative evaluations determined from the CO_2-TPD are summarised in Table 3.

Table 3
CO_2 uptakes for Ru-based catalysts during TPD analysis. The adsorption stage was performed with 5 vol% CO_2 in N_2 from 250 °C to 500 °C.

Sample	Dry tests		Wet tests	
	CO_2 adsorbed ($\mu mol_{CO2}\ g^{-1}$)	CO_2 desorbed ($\mu mol_{CO2}\ g^{-1}$)	CO_2 adsorbed ($\mu mol_{CO2}\ g^{-1}$)	CO_2 desorbed ($\mu mol_{CO2}\ g^{-1}$)
Ru/MgO	145	117	189	148
Ru/MgAl	301	167	357	208
Ru-K/MgAl	429	222	558	299

H_2-TPR analysis was generally conducted on Ru-containing samples to identify the reduction temperature of the metal and study its interaction with different supports. Since the analysis was conducted in an experimental facility equipped with gas analysers, the profiles of H_2 and CH_4 (dot red lines in the figure) were monitored during the experiments. The analysis outputs are depicted in Fig. 6. As reported in the literature, the Ru reduction profile could be affected by several circumstances, such as the interaction between metal and support and/or the dispersion and size of the Ru oxide particles before reduction. Typically, lower temperatures correspond to the reduction of well-dispersed RuO_x species, strongly interacting with the support; instead, RuO_2 phases with a high grade of crystallinity could be reduced at a moderately higher temperature, since these species weakly interact with the supports [25]. The reduction profiles of Ru/MgO (blue line) and Ru/MgAl (green line) catalysts are marked by a sharp single peak centred at 155 and 140 °C, respectively. The tails at the end of the main peak are related to the beginning of methane production. The thermal pretreatment in N_2 flow performed before the H_2-TPR is unable to desorb completely all the carbonates, which remain in the support structures (as confirmed by CO_2-TPD analysis). These carbonate species are activated immediately after the metal phase is entirely reduced, as depicted in Fig. 6. The temperature difference may depend on the above-mentioned factors: ruthenium particles are smaller, well dispersed, and better interacting with the MgAl support than with MgO. Actually, the higher surface area

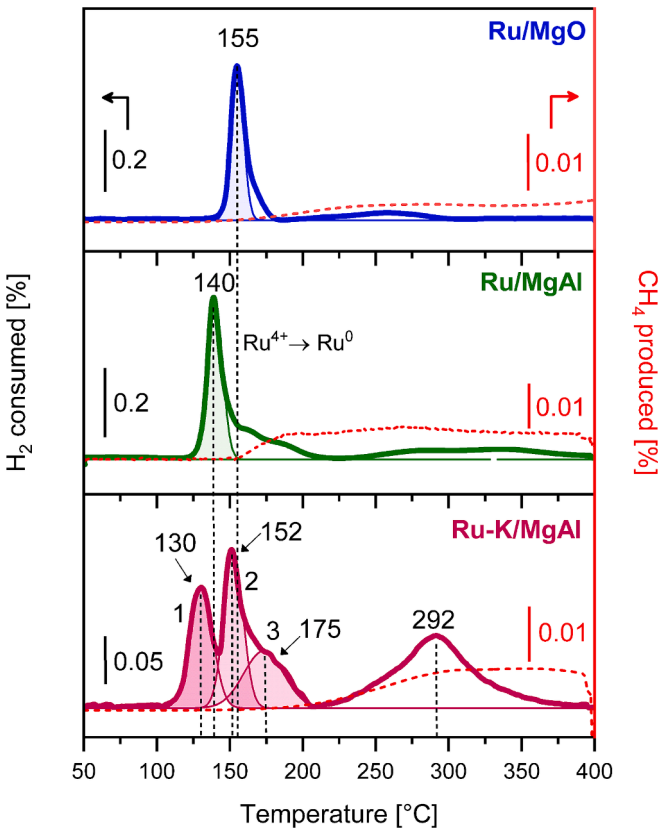

Fig. 6. H_2-TPR profiles of Ru/MgO (solid blue line), Ru/MgAl (solid green line) and Ru-K/MgAl (solid magenta line) catalysts together with the CH_4 production (dash red lines).

of MgAl support could have ensured better metal phase deposition. Otherwise, the reduction of RuO_x species for the Ru-K/MgAl catalyst is characterised by three different contributions at 130, 152 and 175 °C, respectively. Here, the reduction process begins earlier than Ru/MgAl and Ru/MgO samples. This behaviour could be related to the presence of K_2CO_3, which was laid on the surface of the MgAl before the ruthenium. Several studies reported in the literature have observed that the presence of alkali metal around the Ru-support interface allows easier reduction of RuO_x as a result of accelerated charge transfer [72–74]. The integration of TPR peaks enables the assignment of the relative quantity of Ru in contact with K because the low-temperature peak is expected to be related to the reduction of the RuO_x species due to the charge transferred from adjacent K atoms. Specifically, the peak called 1 corresponds to 25 % of the total H_2 consumption. This evidence means that about a quarter of the loaded Ru is influenced by the electronic effect of alkali metal. The other two contributions could demonstrate the presence of large agglomerates of RuO_x species poorly distributed on the support, as observed with microscopy analysis (*vide supra*) [75]. It is essential to recall that impregnation with K_2CO_3 significantly changed the area of the MgAl support; therefore, poor distribution of Ru can be expected on this support. In the one-step reduction of RuO_2, the calculation of the H_2-Ru molar ratio (H_2/Ru, defined as the ratio of the total H_2 consumption to the total amount of Ru determined by ICP analysis) enables the validation of the reduction profiles and calculations derived from the metal content in the sample [76]. The full reduction of RuO_2 requires two moles of H_2. Consequently, a ratio of 2 signifies that the hydrogen utilised corresponds to the complete conversion of the oxide to metallic Ru. All hydrogen consumption occurring at temperatures above 200 °C is considered to be caused by methanation, as mentioned above. In this instance, the hydrogen consumption is stoichiometrically aligned with the amount of methane produced, specifically four times the quantity of CH_4. Table 4 includes the amount of H_2 consumed for Ru reduction, the H_2 consumption for methane production and the amount of methane obtained during the TPR for each catalyst.

3.3. *Operando* FTIR analysis of cyclic methanation

In order to gain a better understanding of the surface intermediates involved in CO_2 capture and methanation processes, a time-resolved *operando* FTIR study was performed on the most promising materials, namely Ru/MgAl and Ru-K/MgAl. The temporal evolution of the IR signals associated with surface species is depicted in Fig. 7. During CO_2 adsorption, the appearance of bands associated with gaseous CO_2 (2400–2250 cm^{-1}) and the symmetric/asymmetric stretching O-C-O vibrations typical of carbonate species was distinctly detected for both catalysts in the 1800 to 1200 $cm^{-}1$ spectral range. Several factors, including the polarising power of metal cations, the material's composition, the presence of water, and/or cations external to the metal's coordination sphere can make carbonate species identification particularly challenging [77,78]. At the beginning of the adsorption step, Ru/MgAl (Fig. 7**A**) was characterised by the appearance of bicarbonate species (HCO_3*), recognisable from the peaks at 1675 cm^{-1} and 1223 cm^{-1}. The first signal is related to O-C-O stretching, while the second is to the C-OH bending mode (δ_{OH}) [44,79–85]. Around 1530 cm^{-1} we can detect a signal attributable to the asymmetric vibration of monodentate carbonate species (ν_{asym} O-C-O); the presence of this species is confirmed by the symmetric vibration (ν_{sym} O-C-O) observed around 1407 cm^{-1} ($\Delta\nu_3$ = 123 cm^{-1}) [25,79,81,83]. Lastly, a very weak signal at 1065 cm^{-1} could be ascribable to overlapping contributions of the monodentate, chelating bidentate and bridged bidentate carbonates [76,83,85]. As time progresses, all these signals increase in intensity with the progressive saturation. Subsequently, the series of spectra (in red in Fig. 7) collected over the successive 30 min under a flow of 5 % H_2 in N_2, exhibited a progressive decrease of carbonate species and an increase in the features associated with metallic carbonyl species. The evolution of signals in the 2100 to 1800 cm^{-1} spectral range is depicted in **panel a-3**. The weak band centred at 2027 cm^{-1} could be assigned to linear CO adsorbed on metallic Ru^0 (νC-O). Various types of CO bond vibrations may have contributed to the formation of a broad asymmetric peak within the spectral range of 2000 cm^{-1} to 1850 cm^{-1} [86,87]. The

Table 4
Summary of the H_2-TPR analysis outputs. The metal percentage reduction is indicated next to the peak temperature.

Sample	$Ru^{4+}\rightarrow Ru^0$ (a)	$Ru^{4+}\rightarrow Ru^0$ (a)	Peak position	H_2/Ru (a)	H_2 consumed (CH_4 production)	CH_4 produced
	Measured consumption $\mu mol_{H_2}\ g^{-1}$	Theoretical consumption $\mu mol_{H_2}\ g^{-1}$	°C		$\mu mol_{H_2}\ g^{-1}$	$\mu mol_{CH_4}\ g^{-1}$
Ru/MgO	23.0	22.5	155 (100 %)	2.0	151.0	38.6
Ru/MgAl	27.3	26.6	140 (100 %)	2.1	313.5	76.8
Ru-K/MgAl	27.3	27.4	130 (25.42 %) 152 (48.10 %) 175 (26.48 %)	2.0	257.6	63.9

(a) Calculations were conducted based on the amount of Ru determined by ICP analysis.

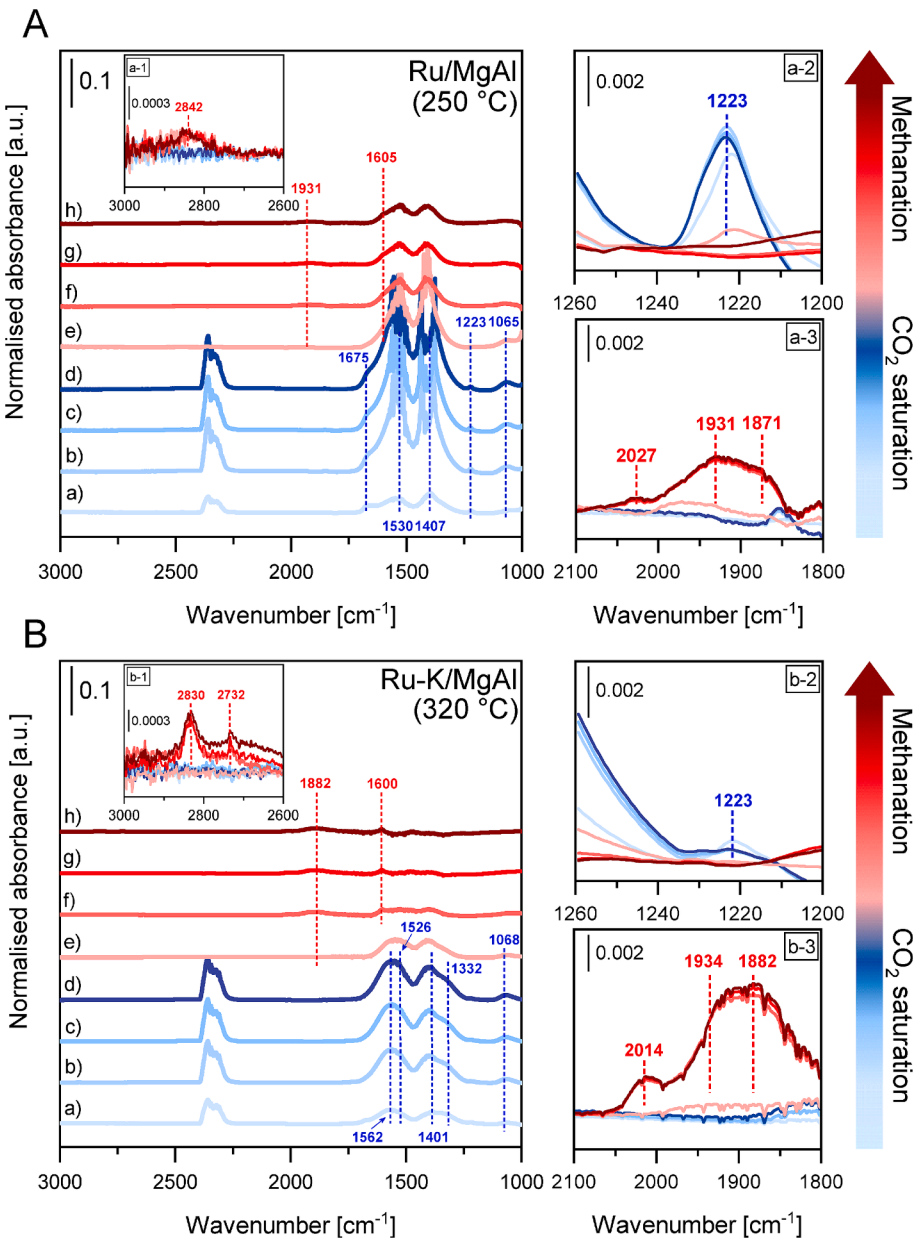

Fig. 7. Representative evolution of the operando FTIR spectra collected during the CO_2 capture/reduction cycle with the catalysts A) Ru/MgAl and B) Ru-K/MgAl. The sequence of the spectra is as follows: a) CO_2 adsorption at 0 min; b) at 10 min; c) at 20 min; d) at 30 min; e) reduction at 0 min; f) at 10 min; g) at 20 min; and h) at 30 min. Magnifications of significant bands are shown in the insets.

literature identifies the spectral range between 1950 and 1900 cm^{-1} as indicative of the CO stretching of the bridged carbonyl on two ruthenium atoms [79,82,84,88–90]. The signals responsible for the terminal tail of the peak (below 1900 cm^{-1}) could be attributed to the presence of polycarbonyl species bonded on Ru species (νC-O species) [84,91–93]. Finally, the signal observed at 1605 cm^{-1} could be related to a modest formation of formate species, intermediates in the methanation reaction (ν_{asym}O-C-O) [84,94]. Additional evidence for the presence of these species is indicated by the peak at 2842 cm^{-1}, which is characteristic of the vC-H stretching in formates (**panel a-1**) [44,79,88,90,94].

Most of the aforementioned features can be applied to the description of spectra corresponding to Ru-K/MgAl (Fig. 7**B**), with minor exceptions. During the adsorption step, alongside the characteristic signals of monodentate carbonate species (1526–1401 cm^{-1}, $\Delta\nu_3 = 125$ cm^{-1}), we can also observe the presence of bidentate carbonates (1562–1332 cm^{-1}, $\Delta\nu_3 = 230$ cm^{-1}) [83,90]. Similar to Ru/MgAl, the Ru-K/MgAl sample also exhibits a signal at 1068 cm^{-1}, which can be attributed to the overlapping of various carbonate species. Conversely, the Ru-K/MgAl sample exhibits no characteristic signals of bicarbonate species, except for a very weak signal observed at 1223 cm^{-1}, as shown in **panel b-2.** The absence of bicarbonates can be attributed to the neutralisation of hydroxyl groups on the MgAl surface, a consequence of alkaline promotion. These hydroxyl groups, which facilitate the formation of bicarbonate species through reaction with CO_2, are effectively neutralised by the K-doping process [90,94,95].

Further distinctions between the two catalysts were observed upon introducing the hydrogen feed. **In panel b-1**, the 3000 to 2600 cm^{-1} spectral range is magnified. The new bands at 2830 and 2732 cm^{-1}, respectively corresponding to νC-H vibration modes, are likely related to the formation of formate (HCOO*) and formyl species (HCO*) as intermediates in the reaction. These species are generated either directly on the metallic surface or at the metal-support interface, where they are subsequently hydrogenated to CH_x species [44,79,88,90,94]. Further evidence for the formation of formate species is provided by the signal

observed at 1600 cm^{-1}, attributed to the asymmetrical ν_{asym}O-C-O stretching vibration of the aforementioned species [25,44,84,88,89,96]. In the spectral region associated with carbonyl vibrations (**panel b-3**), the signal at 2014 cm^{-1}, attributable to CO species bound directly to Ru^0 metal, is distinctly identifiable. As previously discussed, the prominent signal observed below 2000 cm^{-1} may originate from various species, including CO adsorbed in bridged and polyconfiguration across Ru atoms. The greater relative intensity of the CO band in Ru-K/MgAl compared to Ru/MgAl may also be attributed to the presence of carbonyls significantly influenced by K^+ (at frequencies below 1972 cm^{-1}). This may suggest a possible active role of potassium during the hydrogenation phase with reactive KO_x species, as also observed by Lee and Otomo [97]. For the sake of clarity, the assignments of IR signals on the two catalysts are summarised in Table 5. The evolution of the methane concentration in the outlet of the *operando* FTIR cell during the hydrogenation step is depicted in **Figure S3** in the *Supporting Information file*. The catalysts were effective in exhibiting activity, as evidenced by a distinct methane production signal, regardless of the infrared cell configuration.

According to the data obtained from time-resolved *operando* FTIR experiments, Scheme 2 proposes the possible reaction pathways established for CO_2 methanation. In the case of Ru/MgAl, the starting point requires the participation of surface hydroxyls in the reaction with CO_2 to form bicarbonates. Subsequently, the carbonates formed can form formate species, as detected around 1600 cm^{-1}. This pathway ends with the hydrogenation of carbon atoms on Ru. Concerning Ru-K/MgAl, the reaction follows a different route due to the absence of hydroxyl groups, which are necessary for forming bicarbonates. The carbonates undergo hydrogenation to formates, which can subsequently decompose into formyl species and finally in CO and water. As stated before, K^+ species participate in the CO_2 activation, as the intense CO band testified. This pathway ultimately follows the same course as observed in the case of Ru/MgAl.

The results of this time-resolved *operando* FTIR study, aimed at elucidating the underlying mechanisms and reaction intermediates, are in line with the catalytic behaviours subsequently observed (*vide infra*). Distinct species were detected on each catalyst. The formation of bicarbonates, which are partially hydrogenated, on the Ru/MgAl surface may facilitate the migration of these species toward the Ru centres. Furthermore, it is essential to consider that the methanation process occurring on the surface of Ru-K/MgAl includes an additional step where formates must generate formyl species before degrading to CO. This extra step could further reduce the surface reactivity of the latter catalyst.

3.4. Catalytic activity

Cyclic methanation tests were carried out according to the procedure schematised in Fig. 1. At the beginning of the test, the catalysts underwent a thermal activation at 400 °C and a reducing treatment, to clean properly the surface and simultaneously reduce RuO_2 to Ru^0. Then, multiple cycles of CO_2 adsorption and hydrogenation were performed. According to the CO_2-TPD outcomes, the following operating temperatures were adopted: 250 °C for Ru/MgO and Ru/MgAl catalysts, and 320 °C for Ru-K/MgAl. The findings are reported through bar graphs in Fig. 8 and numerically in Table 6. As expected, all ruthenium-functionalised catalysts were active for CO_2 methanation, with 100 % selectivity to methane during the hydrogenation step.

The Ru/MgO catalyst showed a reproducible performance in the cycles, producing a maximum of 99 μmol g^{-1} of CH_4 under dry conditions (Fig. 8**A**) and 106.2 μmol g^{-1} under wet conditions (Fig. 8**B**). These results confirm the data obtained with CO_2-TPD: in the presence of moisture, hydroxyl intermediates are formed, allowing greater carbonation of gaseous CO_2. Wet tests proved that these carbonates are only partially available since the increase in methane production was slight. Under dry conditions, a good carbon balance was achieved, with methane yields above 80 %; in contrast, tests in wet conditions showed a lower yield (on average 58 %) due to unconverted CO_2, which was lost during the purge and hydrogenation steps.

These initial results prompted us to conceive and create Ru-based catalysts with a greater dispersion of the Mg-O species. As mentioned above, the configuration of MgAl materials guarantees this requirement. Ru/MgAl underwent a total of five continuous adsorption and regeneration cycles under dry conditions (Fig. 8**C**) and five under wet conditions (Fig. 8**D**). As predicted by CO_2-TPD, the capture capabilities of this material are better than pure MgO, and this was linked to improved methane production. Generally, the catalyst reached a certain stability between adsorbed and converted CO_2 by the third cycle, achieving an average yield of 85 %. The best cycle was the second, during which Ru/MgAl captured about 228 μmol g^{-1} of CO_2 and produced about 183 μmol g^{-1} of CH_4. Moreover, CO production was noted during the CO_2 adsorption phase. This phenomenon can be due to the presence of residual H_2 from the reduction step that may have remained as hydrides on Ru. In this condition, a partial reduction of CO_2 occurs with the production of CO, in contrast to the hydrogenation phase, when hydrogen is the excess reactant.

In wet conditions, both adsorptive and catalytic capacities improved. Of all, the best cycle was the first one with 361 μmol g^{-1} of CO_2 captured and 220 μmol g^{-1} of CH_4 produced. The average yield was lower (79 %)

Table 5
Summary of the species formed during CO_2 saturation and the subsequent methanation reaction for Ru/MgAl and Ru-K/MgAl catalysts.

Sample	Frequency (cm^{-1})	Surface species	Vibration[(a)]	References
Ru/MgAl	1065	Overlapping of various carbonate species	ν_{sym}C-O	[76,83,85]
	1223	Bicarbonate species (HCO_3*)	δ_{OH}	[44,79–85]
	1411	Monodentate carbonate	ν_{sym}O-C-O	[25,79,81,83]
	1530	Monodentate carbonate	ν_{asym}O-C-O	[25,79,81,83]
	1605	Formate (HCOO*)	ν_{asym}O-C-O	[84,94]
	1675	Bicarbonate species (HCO_3*)	ν_{asym}O-C-O	[44,79–85]
	2000–1850	Polycarbonyls and carbonyls bridged with Ru atoms	νC-O	[79,82,84,86–93]
	2027	Linear CO_{ads} on metallic Ru^0	νC-O	
	2842	Formate (HCOO*)	νC-H	[44,79,88,90,94]
Ru-K/MgAl	1068	Overlapping of various carbonate species	ν_{sym}C-O	[76,83,85]
	1332	Bidentate carbonate	ν_{sym}O-C-O	[83,90]
	1401	Monodentate carbonate	ν_{sym}O-C-O	[25,79,81,83]
	1526	Monodentate carbonate	ν_{asym}O-C-O	[25,79,81,83]
	1562	Bidentate carbonate	ν_{asym}O-C-O	[83,90]
	1600	Formate (HCOO*)	ν_{asym}O-C-O	[25,44,84,88,89,96]
	2000–1850	Polycarbonyls and carbonyls bridged with Ru atoms (and K^+ species)	νC-O	[79,82,84,86–93,97]
	2014	Linear CO_{ads} on metallic Ru^0	νC-O	
	2732	Formyl (HCO*)	νC-H	[44,79,88,90,94]
	2830	Formate (HCOO*)	νC-H	

(a) Vibrations: ν = stretching, δ = bending.

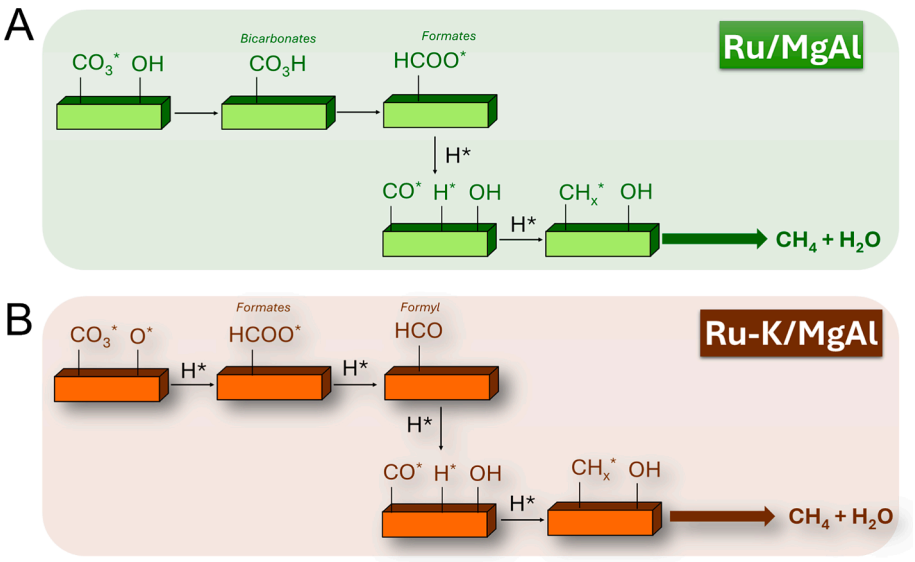

Scheme 2. Schematic representation of the reaction network hypothesised from the spectroscopic outcomes of time-resolved operando FTIR measurements for A) Ru/MgAl and B) Ru-K/MgAl. Figure adapted from Navarro-Jaén et al. [94].

probably for the reasons mentioned above. The doping with K_2CO_3 further enhanced the catalyst's overall performance. Ru-K/MgAl captured 380 μmol g^{-1} of CO_2 and generated 326.5 μmol g^{-1} of CH_4 in its best cycle (the 3rd) of the dry campaign (Fig. 8**E**). The average yield in the five cycles was 85 %. The presence of moisture favoured adsorption in wet tests (Fig. 8**F**), but a corresponding notable increase in methane was not achieved. In the wet campaign, the best cycle was the last one, featuring 487.1 μmol g^{-1} of captured CO_2 and 333.4 μmol g^{-1} of CH_4 generated. the average yield of the 5 cycles was 66 %. Generally, the H_2 consumption during the catalytic methanation was at a 4:1 ratio with CH_4, in line with the stoichiometry of Sabatier's reaction. For the sake of brevity, the results for 10 experiments conducted at 250 °C using the Ru/MgAl catalyst are depicted in **Figure S4** in the *supporting information file*. This campaign further demonstrates the excellent cyclic stability of this catalyst. Compared to the initial five cycles, the methane yields progressively increased, reaching 98 %. The findings are reported numerically in **Table S1** in the *supporting information file*. Lastly, it is reasonable that the discrepancy between adsorbed CO_2 and CH_4 produced may be due to CO_2 desorbing during the purge phase.

Additional tests under dry and wet conditions were conducted at 320 °C on the Ru/MgO and Ru/MgAl catalysts. The findings are presented through bar graphs in **Figure S5** and numerically in **Table S2** in the *supporting information file*. As expected, the increase in temperature negatively affects adsorption, given its exothermic nature. The decrease in adsorbed CO_2 consequently leads to a lower amount of methane produced. For both catalysts, adsorption in the presence of moisture positively affected the performance, even at higher temperatures. It is noteworthy that both catalysts exhibit significant yields even at 320 °C. Ru/MgAl shows the best results, with a maximum of 130.2 μmol g^{-1} of methane in cycle dry-C1 and 178.5 μmol g^{-1} of methane in cycle wet-C1. Methane yields ranging between 80 and 90 % indicate good stability and reproducible performance of the catalyst, even at higher temperatures.

To better understand the catalysts developed in this work, methanation profiles were investigated. As an overview, Fig. 9**A** shows the CH_4 production profiles obtained in the dry and wet experiments. Methane production during dry tests of the Ru/MgO and Ru/MgAl catalysts (blue and green lines) was characterised by a very sharp profile, with a gas peak centred mainly during the first minutes of the reducing phase. The main peak was followed by a tail that reached zero already after 30 min. The presence of moisture in the CO_2 feed led to a slowdown in the reduction rate of methane. This can be inferred by observing the shift and broadening of the CH_4 signals produced for Ru/MgO and Ru/MgAl (light blue and light green lines). This empirical evidence can be rationalised by considering the formation of the carbonate layer in the presence of moisture, as outlined in the CO_2-TPD discussion [65]. Indeed, a thicker layer of carbonate species could hinder its diffusion towards Ru centres, thereby slowing down the rate of methanation.

It is noteworthy to analyse the significant influence of the potassium promoter on the dynamic processes of CO_2 capture and reduction. As stated previously, the adsorption efficiency was considerably increased in the case of K doping, as well as its conversion to methane. However, conversely, to the other Ru-catalysts, Ru-K/MgAl displayed an enlarged profile with a maximum methane production after 5 min of reduction. Moreover, the reduction time is remarkably longer: the other catalysts achieved 90 % of the methane produced in 10 min, while Ru-K/MgAl lasted more than 30 min. This behaviour was further exacerbated after adsorption of wet CO_2, when, instead of a distinct peak, a broad curve terminating after 80 min was observed.

The findings from tests and characterisations suggest a mechanistic hypothesis that can provide a more comprehensive explanation, as schematised in Fig. 9**B**. Initially, CO_2 adsorbs to form carbonates. These species interact with dissociative adsorbed H_2 on the Ru surface, forming CH_4. For Ru/MgAl and Ru/MgO, decomposition and conversion occur faster during the hydrogenation step (**Scenario a**). Instead, the interaction between CO_2 and the stronger alkaline sites of Ru-K/MgAl led to the formation of more stable carbonates, thus hindering their diffusion towards the Ru species (**Scenario b**). Indeed, Sun et al. [33] observed a slow desorption rate for hydrotalcite-doped alkali metal carbonate, attributed to the high stability of $K_2Mg(CO_3)_2$. This characteristic could have further influenced the shape of the methane profile of Ru-K/MgAl. This phenomenon may have been further promoted by the lower surface area and the poor Ru distribution.

Actually, the scientific literature is divided regarding the effect of potassium doping. Similar findings were observed by García-Bordejé et al. [98] who scrutinised Ni and Ru-based catalysts for CO_2 hydrogenation. To improve the adsorption abilities, the authors doped the materials with alkali (Na or K) or alkaline earth (Ba) metal. TPSR characterisation evidenced that the catalyst containing barium demonstrates heightened methanation kinetics of CO_x adsorbed species compared to catalysts containing potassium or sodium. Besides, other research groups have prepared potassium-doped catalysts, observing detrimental consequences on CO_2 methanation. In the study conducted

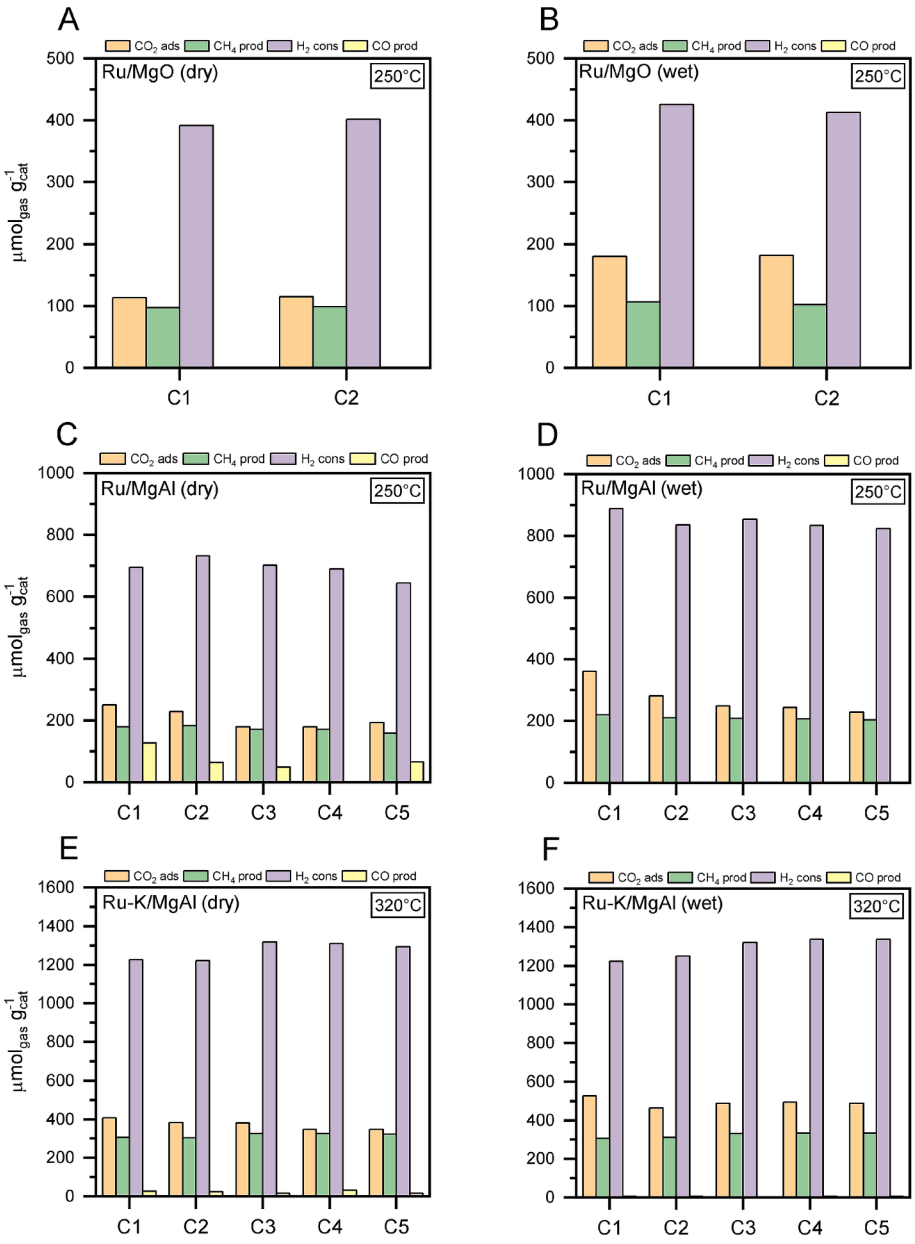

Fig. 8. Summary of the results of catalytic activity tests. The orange bars represent the CO_2 adsorbed during the adsorption step, the violet bars the H_2 consumed during the hydrogenation step, the yellow bars the CO generated during the adsorption step, and the green bars the CH_4 produced. Cx reported in the x-axes refers to the number of cycles.

by Büchel et al. [99], the CO_2 hydrogenation process was investigated using K- and Ba-modified 1 % Rh/Al_2O_3 catalysts. Unfortunately, catalytic tests evidenced the exclusive production of CO across all temperature ranges. The modification of 15 % Co/SiO_2 with 1–5 wt% K was further investigated by Iloy et al. [100]. It was demonstrated that the K dopant enhanced CO_2 chemisorption while favouring CO selectivity and promoting C-C coupling along with chain growth reactions. In another study, Cimino et al. [101] investigated the consequences of incorporating alkali metals (e.g., Li, Na, K) into a Ru-based catalyst for CO_2 methanation. Catalytic experiments pointed out the adverse impact of K_2CO_3 doping on the catalytic performances, caused by Ru masking by alkali metal.

On the other hand, Duyar et al. [102] observed a doubling of the catalyst's methanation capacity when impregnated with K_2CO_3 or Na_2CO_3. They ascribed the beneficial effect of doping to the interaction between the carbonate and the hydrogen escaping from the noble metal. Similar conclusions were reported in a study by Tsuneto et al. [103]. In recent work, Jo et al. [69] developed a Ru/K_2CO_3-MgO dual-function material for integrated CO_2 capture and methanation, achieving stable CH_4 productivity thanks to the beneficial interaction between all the catalyst components Also, Lee and Otomo [97] discovered a promotional effect of K on β″ alumina catalyst for methanation reaction. Diffuse reflectance FTIR spectroscopy showed that potassium ions in K-β″ alumina play an active role in the generation of intermediates (CO_3^{2-} and CO). The enhancement in reactions is attributed to $\sigma \rightarrow \pi$ potassium back donation, facilitating their interaction with other intermediates (formate and carbonyl). Similarly to the present work, Hu and Urakawa [104] observed that upon K-promotion (Ni-K/ZrO_2), both CO_2 conversion and CH_4 selectivity improved drastically. Nevertheless, they found a remarkable increase in reduction time compared to other catalysts. The K-promotion modified the reaction mechanism: formyl species in conjunction with bidentate carbonates became the active surface species, which are more resistant to reduction by H_2 into CH_4. The latter observation aligns with the results obtained here by *operando* FTIR,

Table 6
Summary of the catalytic results in terms of CO_2 adsorbed and CO produced during the adsorption step, CH_4 produced and H_2 consumed during the hydrogenation step, and the yield in percentage during the experimental campaigns (d = dry adsorption, w = wet adsorption, Cx = number of cycles).

Catalyst	No. Test	CO_2 adsorbed (**μmol g^{-1}**)	CH_4 produced (**μmol g^{-1}**)	H_2 consumed (**μmol g^{-1}**)	CO produced (**μmol g^{-1}**)	Yield (%)
Ru/MgO	d-C1	113.4	96.9	391.7	0.0	85
	d-C2	114.9	99.0	401.6	0.0	86
	w-C1	180.1	106.2	425.7	0.0	59
	w-C2	181.8	102.7	412.8	0.0	56
Ru/MgAl	d-C1	249.9	179.9	695.6	126.5	72
	d-C2	227.8	182.9	733.5	64.2	80
	d-C3	179.8	171.5	702.3	48.5	95
	d-C4	180.1	170.7	691.1	0.0	95
	d-C5	192.6	159.6	644.1	66.6	83
	w-C1	361.1	220.2	888.7	0.0	61
	w-C2	282.0	209.3	835.2	0.0	74
	w-C3	249.4	208.9	853.7	2.2	84
	w-C4	243.7	207.1	834.5	1.8	85
	w-C5	228.8	202.7	823.0	2.0	89
Ru-K/MgAl	d-C1	406.1	305.6	1224.8	26.6	75
	d-C2	382.4	304.0	1219.8	24.1	80
	d-C3	380.3	326.5	1318.3	15.3	86
	d-C4	348.1	324.9	1309.7	32.5	93
	d-C5	347.9	323.1	1292.7	16.2	93
	w-C1	526.2	305.7	1223.1	4.8	58
	w-C2	463.4	312.6	1251.3	5.7	67
	w-C3	489.1	330.5	1322.0	0.0	68
	w-C4	493.7	332.5	1336.7	5.0	67
	w-C5	487.1	333.4	1336.7	6.4	68

through which bidentate formyl and carbonate species were detected on the potassium-doped sample.

For comparison purposes, integrated CO_2 capture and reduction performances previously reported in the literature are listed in Table 7. Notably, most catalysts documented in the literature possess an active metal phase (Ru or Ni or both) exceeding 5 wt%. Furthermore, commercial catalysts also typically exhibit an active phase content of at least 5 wt%. Consequently, an adequate comparison of the materials synthesised in this study with literature models proves challenging. However, it remains a fact that the specific methane productivity (μmol_{CH4} g^{-1}) of our catalysts is substantial, given the low loading of deposited Ru, even under highly realistic reaction conditions. The catalysts presented in this study demonstrate significant competitiveness with those documented in the literature, particularly when evaluating the amount of methane produced per gram of active metal. Moreover, it is also essential to take into account the CO_2 concentration during adsorption and the time required for regeneration with H_2. Often, the partial pressure of CO_2 used in many works exceeds that employed in this work. A higher percentage of CO_2 can increase the adsorption capacity and, consequently, also the methane yield. Finally, process intensification is determined by the length of the reduction period and the length of the CO_2 capture period. The durations for CO_2 capture and reduction should be matched when two reactors are employed to operate continuously by switching their functions (capture or reduction). Considering this purpose, Ru-K/MgAl seems to be ill-suited since the reduction time is remarkably longer than the full CO_2 adsorption duration under the condition evaluated. This would imply switching to the adsorption phase when the material is not yet fully regenerated, affecting the efficiency of subsequent capture. Instead, Ru/MgAl performs more suitably for the final application, since there would be symmetry between the capture and reduction periods. Additionally, the shorter reduction period results in a more efficient use of H_2 by decreasing the amount of unreacted H_2 that is released in the effluent. Finally, it is noteworthy to emphasise that the catalysts examined in this study are notably cost-effective. Through a straightforward heat treatment, a substrate with significant alkaline properties and a high surface area can be produced. The ruthenium precursor constitutes the most expensive component of the entire catalyst. Nevertheless, our findings demonstrate that a competitive catalyst can be achieved by reducing the amount of deposited metal. Given these considerations, it can be concluded that MgAl-based catalysts are competitive due to their excellent performance, even with a low Ru content, and their low cost and straightforward production process.

4. Conclusions

Ru catalysts supported on MgO and Mg-Al-based Layered Double Oxides were investigated for consecutive CO_2 adsorption (in dry and wet conditions) and methanation at atmospheric pressure. Physico-chemical characteristics (e.g., CO_2-TPD, N_2 physisorption at −196 °C, etc.) highlighted the fundamental effect of active site dispersion (Mg^{2+} – O^{2-}) and surface area in the adsorption step, which greatly favoured the capture capacity of the Ru/MgAl catalyst. We confirmed the positive influence of moisture in the carbonation of carbon dioxide gas. Moreover, doping with K_2CO_3 further enhanced capture performance, despite a significant loss of surface area. All three catalysts demonstrated excellent methane conversion capability and selectivity over multiple operating cycles. Methane yields were substantial considering the relatively low Ru content compared to reference materials in the literature. The characterisations and experimental tests proved that a more defective material with greater dispersion of the adsorbent phase (i.e., MgAl) also allowed a considerable increase in the total methane production capacity. Ru-K/MgAl demonstrated different conversion kinetics, as shown by the analysis of CH_4 profiles: the presence of the alkali metal considerably slows down the rate of migration of carbonates towards the reactive centres. This phenomenon could be related to several factors, such as the poor dispersion of Ru (as evidenced by microscopic analysis), the low surface area (nitrogen physisorption) and the significant carbonation strength increased by K_2CO_3 (CO_2-TPD). Additionally, *operando* FTIR tests revealed differences in the reaction intermediates for the two catalysts. This finding may account for the variations in methanation kinetics observed between Ru/MgAl and Ru-K/MgAl. Among the three materials examined in this study, the Ru/MgAl catalyst demonstrated promising performances, due to both high adsorption capacity and its ability to operate within symmetrical cycles, thereby minimising hydrogen wastage. This study aimed to highlight the potential of bifunctional materials for the in situ capture and conversion of CO_2. Although the capture process occurs at high temperatures, which

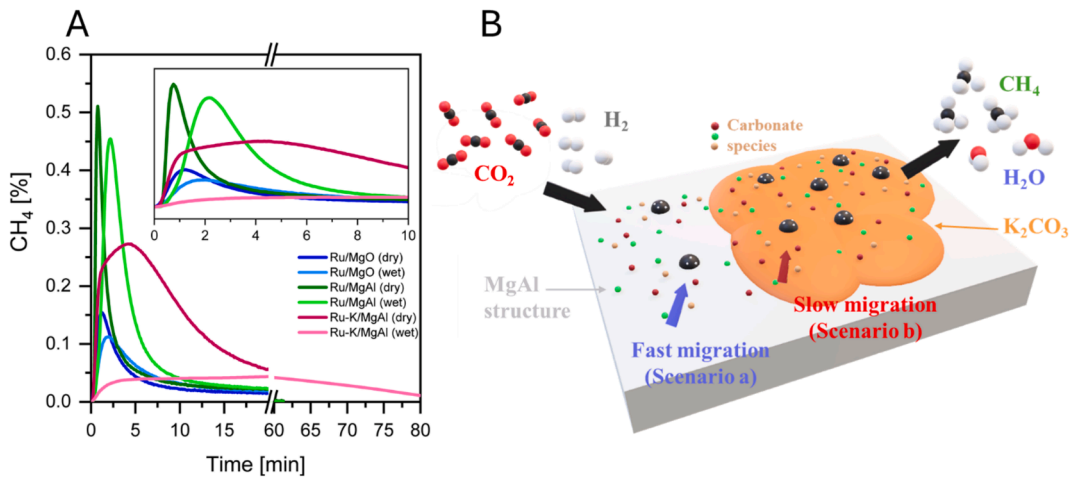

Fig. 9. A) Evolution of methane produced during the hydrogenation phase of the catalytic tests in dry and wet conditions. B) Proposed mechanism for the different methane profiles.

Table 7
Summary of some CO_2 capture and reduction efficiencies of Ru-based catalysts previously documented and those discussed in our current research.

Catalyst	Adsorption parameters	Methanation parameters	Highest CH_4 production ($\mu mol_{CH4}\ g^{-1}_{cat}$)	Activity per active metal ($mmol_{CH4}\ g^{-1}_{active\ metal}$)	Ref
5 % Ru, 10 % CaO/Al_2O_3 100 mg	10 % CO_2/N_2, 320 °C, 30 min	4 % H_2/N_2, 320 °C, 2 h	500	10.0	[105]
5 % Ru, 6.1 % Na_2O/Al_2O_3 100 mg	10 % CO_2/N_2, 320 ∘C, 30 min	10 % H_2/N_2, 320 °C, 1 h	614	12.3	[22]
1 % Ru, 10 % Ni, 6.1 % Na_2O/Al_2O_3 1 g	7.5 % CO_2, 4.5 % O_2, 15 % H_2O/N_2, 320 °C, 20 min	15 % H_2/N_2, 320 °C (time not reported)	380	3.5	[106]
0.5 % Ru, 5 % Ni, 6.1 % Na_2O/Al_2O_3 10 g	7.5 vol% CO_2, 4.5 vol% O_2, and 10 vol% H_2O, 320 °C, 10 min	15 vol% H_2 10 min	280	5.1	[107]
2 % Ru, 20 % K_2CO_3/MgAl 400 mg	5 % CO_2/N_2, 320 °C (+10 % RH), 30 min	5 % H_2/N_2, 320 °C, up to 1 h	327 (dry) – 333 (wet)	16.3 (dry) – 16.6 (wet)	Present work
2 %Ru/MgAl 400 mg	5 % CO_2/N_2, 250 °C (+10 % RH), 30 min	5 % H_2/N_2, 250 °C, up to 1 h	180 (dry) – 220 (wet)	9.2 (dry) – 11.3 (wet)	Present work
2 %Ru/MgO 400 mg	5 % CO_2/N_2, 250 °C (+10 % RH), 30 min	5 % H_2/N_2, 250 °C, up to 1 h	99 (dry) – 106 (wet)	6.6 (dry) – 7.1 (wet)	Present work

may reduce the performance of the adsorbent component, maintaining an isothermal system enhances the overall efficiency of the process. The heat generated by the reaction (approximately 165 kJ per mole of CO_2) allows for effective carbon dioxide activation without the need for additional energy input. Further optimization of this system can lead to the production of cost-effective and health-safe catalysts, competitive with conventional materials, enabling the development of new technologies for the capture and utilisation of CO_2 emitted by industrial plants.

CRediT authorship contribution statement

Andrea Rizzetto: Investigation, Formal analysis, Data curation. **Enrico Sartoretti:** Investigation, Formal analysis. **Marco Piumetti:** Project administration, Investigation, Funding acquisition. **Raffaele Pirone:** Data curation, Conceptualization. **Samir Bensaid:** Data curation, Conceptualization.

Declaration of competing interest

The authors declare that they have no known competing financial interests or personal relationships that could have appeared to influence the work reported in this paper.

Acknowledgements

The authors greatly thank Paolo Bonora and Tommaso Cancellieri for helping collect data during their MS thesis preparation. Camilla Galletti is kindly acknowledged as well for performing XRD. Eleonora Calì is kindly acknowledged as well for performing FESEM-EDX acquisitions. This publication is part of the project NODES which has received funding from the MUR - M4C2 1.5 of PNRR funded by the European Union - NextGenerationEU (Grant agreement no. ECS00000036). E.S. acknowledges the PON Ricerca e Innovazione "REACT-EU" project (DM 1062/21). The authors kindly acknowledge METHA (Synthesis of renewable METHAne from CO_2 with advanced and robust catalysts) project funded by Compagnia di San Paolo through Bando "TRAPEZIO – Paving the way to research excellence and talent attraction" Linea 1: sostenere la ricerca competitiva.

Appendix A. Supplementary data

Supplementary data to this article can be found online at https://doi.org/10.1016/j.cej.2024.157585.

Data availability

Data will be made available on request.

References

[1] F. Salomone, G. Bonura, F. Frusteri, M. Castellino, M. Fontana, A.M. Chiodoni, N. Russo, R. Pirone, S. Bensaid, Physico-chemical modifications affecting the activity and stability of cu-based hybrid catalysts during the direct hydrogenation of carbon dioxide into dimethyl-ether, Materials 15 (2022) 7774, https://doi.org/10.3390/ma15217774.

[2] F. Salomone, E. Sartoretti, S. Ballauri, M. Castellino, C. Novara, F. Giorgis, R. Pirone, S. Bensaid, CO2 hydrogenation to methanol over Zr- and Ce-doped indium oxide, Catal. Today 423 (2023) 114023, https://doi.org/10.1016/j.cattod.2023.01.030.

[3] M.P. Mezzapesa, F. Salomone, H. Guzmán, F. Zammillo, R. Millini, L. Bua, G. Marra, A. Tacca, R. Marrazzo, N. Russo, R. Pirone, S. Hernandez, S. Bensaid, Development of In-Cu binary oxides catalysts for hydrogenating CO2 via thermocatalytic and electrocatalytic routes, Inorg. Chem. Front. (2024), https://doi.org/10.1039/D3QI02499G.

[4] E. Corrao, F. Salomone, E. Giglio, M. Castellino, S.M. Ronchetti, M. Armandi, R. Pirone, S. Bensaid, CO2 conversion into hydrocarbons via modified Fischer-Tropsch synthesis by using bulk iron catalysts combined with zeolites, Chem. Eng. Res. Des. 197 (2023) 449–465, https://doi.org/10.1016/j.cherd.2023.07.052.

[5] M.H. Albadi, E.F. El-Saadany, Overview of wind power intermittency impacts on power systems, Electr. Pow. Syst. Res. 80 (2010) 627–632, https://doi.org/10.1016/j.epsr.2009.10.035.

[6] D. Connolly, H. Lund, B.V. Mathiesen, E. Pican, M. Leahy, The technical and economic implications of integrating fluctuating renewable energy using energy storage, Renew. Energy 43 (2012) 47–60, https://doi.org/10.1016/j.renene.2011.11.003.

[7] M. Beaudin, H. Zareipour, A. Schellenberglabe, W. Rosehart, Energy storage for mitigating the variability of renewable electricity sources: an updated review, Energy Sustain. Dev. 14 (2010) 302–314, https://doi.org/10.1016/j.esd.2010.09.007.

[8] J.-P. Maton, L. Zhao, J. Brouwer, Dynamic modeling of compressed gas energy storage to complement renewable wind power intermittency, Int. J. Hydrogen Energy 38 (2013) 7867–7880, https://doi.org/10.1016/j.ijhydene.2013.04.030.

[9] C. Graves, S.D. Ebbesen, M. Mogensen, K.S. Lackner, Sustainable hydrocarbon fuels by recycling CO 2 and H 2 O with renewable or nuclear energy, Renew. Sustain. Energy Rev. 15 (2011) 1–23, https://doi.org/10.1016/j.rser.2010.07.014.

[10] W.L. Becker, R.J. Braun, M. Penev, M. Melaina, Production of Fischer–Tropsch liquid fuels from high temperature solid oxide co-electrolysis units, Energy 47 (2012) 99–115, https://doi.org/10.1016/j.energy.2012.08.047.

[11] I. Rossetti, G.F. Mancini, P. Ghigna, M. Scavini, M. Piumetti, B. Bonelli, F. Cavani, A. Comite, Spectroscopic enlightening of the local structure Of VO $_X$ active sites in catalysts for the odh of propane, J. Phys. Chem. C 116 (2012) 22386–22398, https://doi.org/10.1021/jp307031b.

[12] S. Soodi, E. Calì, S. Saini, W.S. Skinner, A.M. Martin, G. Kerherve, M. P. Mezzapesa, S. Bensaid, D.J. Payne, M.S. Duyar, K. Kousi, Exsolved Cu–ZnO interfaces for methanol production from CO $_2$ at atmospheric pressure, J. Mater. Chem. A (2024), https://doi.org/10.1039/D4TA05812G.

[13] G. Gahleitner, Hydrogen from renewable electricity: An international review of power-to-gas pilot plants for stationary applications, Int. J. Hydrogen Energy 38 (2013) 2039–2061, https://doi.org/10.1016/j.ijhydene.2012.12.010.

[14] T. Schaaf, J. Grünig, M.R. Schuster, T. Rothenfluh, A. Orth, Methanation of CO2 - storage of renewable energy in a gas distribution system, Energ Sustain Soc 4 (2014) 2, https://doi.org/10.1186/s13705-014-0029-1.

[15] E. Giglio, A. Lanzini, M. Santarelli, P. Leone, Synthetic natural gas via integrated high-temperature electrolysis and methanation: part I—energy performance, J. Storage Mater. 1 (2015) 22–37, https://doi.org/10.1016/j.est.2015.04.002.

[16] E. Giglio, F.A. Deorsola, M. Gruber, S.R. Harth, E.A. Morosanu, D. Trimis, S. Bensaid, R. Pirone, Power-to-gas through high temperature electrolysis and carbon dioxide methanation: reactor design and process modeling, Ind. Eng. Chem. Res. 57 (2018) 4007–4018, https://doi.org/10.1021/acs.iecr.8b00477.

[17] F. Salomone, P. Marocco, D. Ferrario, A. Lanzini, D. Fino, S. Bensaid, M. Santarelli, Process simulation and energy analysis of synthetic natural gas production from water electrolysis and CO2 capture in a waste incinerator, Appl. Energy 343 (2023) 121200, https://doi.org/10.1016/j.apenergy.2023.121200.

[18] K. Hashimoto, M. Yamasaki, K. Fujimura, T. Matsui, K. Izumiya, M. Komori, A. A. El-Moneim, E. Akiyama, H. Habazaki, N. Kumagai, A. Kawashima, K. Asami, Global CO2 recycling—novel materials and prospect for prevention of global warming and abundant energy supply, Mater. Sci. Eng. A 267 (1999) 200–206, https://doi.org/10.1016/S0921-5093(99)00092-1.

[19] S. Abate, C. Mebrahtu, E. Giglio, F. Deorsola, S. Bensaid, S. Perathoner, R. Pirone, G. Centi, Catalytic performance of γ-Al $_2$ O $_3$ –ZrO $_2$ –TiO $_2$ –CeO $_2$ composite oxide supported Ni-based catalysts for CO $_2$ methanation, Ind. Eng. Chem. Res. 55 (2016) 4451–4460, https://doi.org/10.1021/acs.iecr.6b00134.

[20] J. Gao, Y. Wang, Y. Ping, D. Hu, G. Xu, F. Gu, F. Su, A thermodynamic analysis of methanation reactions of carbon oxides for the production of synthetic natural gas, RSC Adv. 2 (2012) 2358, https://doi.org/10.1039/c2ra00632d.

[21] I. Hussain, A.A. Jalil, N.S. Hassan, M.Y.S. Hamid, Recent advances in catalytic systems for CO2 conversion to substitute natural gas (SNG): perspective and challenges, Journal of Energy Chemistry 62 (2021) 377–407, https://doi.org/10.1016/j.jechem.2021.03.040.

[22] M.A. Arellano-Treviño, Z. He, M.C. Libby, R.J. Farrauto, Catalysts and adsorbents for CO2 capture and conversion with dual function materials: limitations of Ni-containing DFMs for flue gas applications, J. CO2 Util. 31 (2019) 143–151, https://doi.org/10.1016/j.jcou.2019.03.009.

[23] A. Porta, R. Matarrese, C.G. Visconti, L. Castoldi, L. Lietti, Storage material effects on the performance of Ru-based CO $_2$ capture and methanation dual functioning materials, Ind. Eng. Chem. Res. 60 (2021) 6706–6718, https://doi.org/10.1021/acs.iecr.0c05898.

[24] S. Cimino, R. Russo, L. Lisi, Insights into the cyclic CO2 capture and catalytic methanation over highly performing Li-Ru/Al2O3 dual function materials, Chem. Eng. J. 428 (2022) 131275, https://doi.org/10.1016/j.cej.2021.131275.

[25] A. Rizzetto, M. Piumetti, R. Pirone, E. Sartoretti, S. Bensaid, Study of ceria-composite materials for high-temperature CO2 capture and their ruthenium functionalization for methane production, Catal. Today 429 (2024) 114478, https://doi.org/10.1016/j.cattod.2023.114478.

[26] P. Melo Bravo, D.P. Debecker, Combining CO2 capture and catalytic conversion to methane, Waste Dispos Sustain. Energy 1 (2019) 53–65, https://doi.org/10.1007/s42768-019-00004-0.

[27] Y. Guo, C. Tan, P. Wang, J. Sun, W. Li, C. Zhao, P. Lu, Magnesium-based basic mixtures derived from earth-abundant natural minerals for CO2 capture in simulated flue gas, Fuel 243 (2019) 298–305, https://doi.org/10.1016/j.fuel.2019.01.108.

[28] V. Hiremath, H.J. Kwon, I. Jung, S. Kwon, S.H. Kwon, S.G. Lee, H.C. Lee, J.G. Seo, Mg-ion inversion in MgO@MgO−Al $_2$ O $_3$ oxides: the origin of basic sites, ChemSusChem 12 (2019) 2810–2818, https://doi.org/10.1002/cssc.201900072.

[29] W. Gao, T. Zhou, Y. Gao, B. Louis, D. O'Hare, Q. Wang, Molten salts-modified MgO-based adsorbents for intermediate-temperature CO2 capture: a review, Journal of Energy Chemistry 26 (2017) 830–838, https://doi.org/10.1016/j.jechem.2017.06.005.

[30] P. Li, R. Chen, Y. Lin, W. Li, General approach to facile synthesis of MgO-based porous ultrathin nanosheets enabling high-efficiency CO2 capture, Chem. Eng. J. 404 (2021) 126459, https://doi.org/10.1016/j.cej.2020.126459.

[31] S. Abate, K. Barbera, E. Giglio, F. Deorsola, S. Bensaid, S. Perathoner, R. Pirone, G. Centi, Synthesis, characterization, and activity pattern of Ni–Al hydrotalcite catalysts in CO $_2$ methanation, Ind. Eng. Chem. Res. 55 (2016) 8299–8308, https://doi.org/10.1021/acs.iecr.6b01581.

[32] P. Marocco, E.A. Morosanu, E. Giglio, D. Ferrero, C. Mebrahtu, A. Lanzini, S. Abate, S. Bensaid, S. Perathoner, M. Santarelli, R. Pirone, G. Centi, CO2 methanation over Ni/Al hydrotalcite-derived catalyst: experimental characterization and kinetic study, Fuel 225 (2018) 230–242, https://doi.org/10.1016/j.fuel.2018.03.137.

[33] L. Sun, Y. Yang, H. Ni, D. Liu, Z. Sun, P. Li, J. Yu, Enhancement of CO $_2$ adsorption performance on hydrotalcites impregnated with alkali metal nitrate salts and carbonate salts, Ind. Eng. Chem. Res. 59 (2020) 6043–6052, https://doi.org/10.1021/acs.iecr.9b05700.

[34] C.V. Miguel, R. Trujillano, V. Rives, M.A. Vicente, A.F.P. Ferreira, A.E. Rodrigues, A. Mendes, L.M. Madeira, High temperature CO2 sorption with gallium-substituted and promoted hydrotalcites, Sep. Purif. Technol. 127 (2014) 202–211, https://doi.org/10.1016/j.seppur.2014.03.007.

[35] J.M. Silva, R. Trujillano, V. Rives, M.A. Soria, L.M. Madeira, High temperature CO 2 sorption over modified hydrotalcites, Chem. Eng. J. 325 (2017) 25–34, https://doi.org/10.1016/j.cej.2017.05.032.

[36] E.L.G. Oliveira, C.A. Grande, A.E. Rodrigues, CO2 sorption on hydrotalcite and alkali-modified (K and Cs) hydrotalcites at high temperatures, Sep. Purif. Technol. 62 (2008) 137–147, https://doi.org/10.1016/j.seppur.2008.01.011.

[37] X. Zhu, Y. Shi, N. Cai, High-pressure carbon dioxide adsorption kinetics of potassium-modified hydrotalcite at elevated temperature, Fuel 207 (2017) 579–590, https://doi.org/10.1016/j.fuel.2017.06.137.

[38] X. Zhu, C. Chen, Q. Wang, Y. Shi, D. O'Hare, N. Cai, Roles for K2CO3 doping on elevated temperature CO2 adsorption of potassium promoted layered double oxides, Chem. Eng. J. 366 (2019) 181–191, https://doi.org/10.1016/j.cej.2019.01.192.

[39] S. Ballauri, E. Sartoretti, M. Hu, C. D'Agostino, Z. Ge, L. Wu, C. Novara, F. Giorgis, M. Piumetti, D. Fino, N. Russo, S. Bensaid, Praseodymium doping in ceria-supported palladium nanocatalysts as an effective strategy to minimize the inhibiting effects of water during methane oxidation, Appl. Catal. B 320 (2023) 121898, https://doi.org/10.1016/j.apcatb.2022.121898.

[40] S. Ballauri, E. Sartoretti, M. Castellino, M. Armandi, M. Piumetti, D. Fino, N. Russo, S. Bensaid, Mesoporous ceria and ceria-praseodymia as high surface area supports for Pd-based catalysts with enhanced methane oxidation activity, ChemCatChem 16 (2024) e202301359.

[41] C. Cocuzza, E. Sartoretti, C. Novara, F. Giorgis, S. Bensaid, N. Russo, D. Fino, M. Piumetti, Copper-manganese oxide catalysts prepared by solution combustion synthesis for total oxidation of VOCs, Catal. Today 423 (2023) 114292, https://doi.org/10.1016/j.cattod.2023.114292.

[42] N. Grifasi, E. Sartoretti, D. Montesi, S. Bensaid, N. Russo, F.A. Deorsola, D. Fino, C. Novara, F. Giorgis, M. Piumetti, Mesostructured manganese oxides for efficient catalytic oxidation of CO, ethylene, and propylene at mild temperatures: insight into the role of crystalline phases and physico-chemical properties, Applied Catalysis B: Environment and Energy 362 (2025) 124696, https://doi.org/10.1016/j.apcatb.2024.124696.

[43] W. Gao, T. Zhou, Q. Wang, Controlled synthesis of MgO with diverse basic sites and its CO2 capture mechanism under different adsorption conditions, Chem. Eng. J. 336 (2018) 710–720, https://doi.org/10.1016/j.cej.2017.12.025.

[44] S. Xu, S. Chansai, Y. Shao, S. Xu, Y. Wang, S. Haigh, Y. Mu, Y. Jiao, C.E. Stere, H. Chen, X. Fan, C. Hardacre, Mechanistic study of non-thermal plasma assisted CO2 hydrogenation over Ru supported on MgAl layered double hydroxide, Appl Catal B 268 (2020) 118752, https://doi.org/10.1016/j.apcatb.2020.118752.

[45] A. Misol, I. Giarnieri, F. Ospitali, A. Ballarini, J. Jiménez-Jiménez, E. Rodríguez-Castellón, F.M. Labajos, G. Fornasari, P. Benito, CO2 hydrogenation over Ru hydrotalcite-derived catalysts, Catal. Today 425 (2024) 114362, https://doi.org/10.1016/j.cattod.2023.114362.

[46] M. Piumetti, B. Bonelli, P. Massiani, S. Dzwigaj, I. Rossetti, S. Casale, L. Gaberova, M. Armandi, E. Garrone, Effect of vanadium dispersion and support properties on the catalytic activity of V-SBA-15 and V-MCF mesoporous materials prepared by direct synthesis, Catal. Today 176 (2011) 458–464, https://doi.org/10.1016/j.cattod.2010.10.066.

[47] M. Piumetti, M. Armandi, E. Garrone, B. Bonelli, An IR spectroscopy assessment of the surface acidity of mesoporous VO –SiO2 catalysts, Microporous Mesoporous Mater. 164 (2012) 111–119, https://doi.org/10.1016/j.micromeso.2012.05.041.

[48] M. Argyle, C. Bartholomew, Heterogeneous catalyst deactivation and regeneration: a review, Catalysts 5 (2015) 145–269, https://doi.org/10.3390/catal5010145.

[49] F. Cavani, F. Trifirb, A. Vaccari, Hydrotalcite-type anionic clays: Preparation, properties and applications, Catal. Today 11 (1991) 173–301, https://doi.org/10.1016/0920-5861(91)80068-k.

[50] L.K.G. Bhatta, S. Subramanyam, M.D. Chengala, U.M. Bhatta, K. Venkatesh, Enhancement in CO $_2$ adsorption on hydrotalcite-based material by novel carbon support combined with K $_2$ CO $_3$ impregnation, Ind. Eng. Chem. Res. 54 (2015) 10876–10884, https://doi.org/10.1021/acs.iecr.5b02020.

[51] P. Li, M. Zhu, Z. Tian, Y. Han, Y. Zhang, T. Zhou, L. Kang, J. Dan, X. Guo, F. Yu, Q. Wang, B. Dai, Two-dimensional layered double hydroxide derived from vermiculite waste water supported highly dispersed Ni nanoparticles for CO methanation, Catalysts 7 (2017) 79, https://doi.org/10.3390/catal7030079.

[52] W. Yang, Y. Kim, P.K.T. Liu, M. Sahimi, T.T. Tsotsis, A study by in situ techniques of the thermal evolution of the structure of a Mg–Al–CO3 layered double hydroxide, Chem. Eng. Sci. 57 (2002) 2945–2953, https://doi.org/10.1016/S0009-2509(02)00185-9.

[53] M. Thommes, K. Kaneko, A.V. Neimark, J.P. Olivier, F. Rodriguez-Reinoso, J. Rouquerol, K.S.W. Sing, Physisorption of gases, with special reference to the evaluation of surface area and pore size distribution (IUPAC Technical Report), Pure Appl. Chem. 87 (2015) 1051–1069, https://doi.org/10.1515/pac-2014-1117.

[54] M. Piumetti, F.S. Freyria, M. Armandi, F. Geobaldo, E. Garrone, B. Bonelli, Fe- and V-doped mesoporous titania prepared by direct synthesis: Characterization and role in the oxidation of AO7 by H2O2 in the dark, Catal. Today 227 (2014) 71–79, https://doi.org/10.1016/j.cattod.2013.11.013.

[55] N. Grifasi, F.A. Deorsola, D. Fino, M. Piumetti, Mesoporous TiO2 and Fe-containing TiO2 prepared by solution combustion synthesis as catalysts for the photodegradation of paracetamol, Environ Sci Pollut Res (2024), https://doi.org/10.1007/s11356-024-33575-5.

[56] S. Kim, S.G. Jeon, K.B. Lee, High-temperature CO $_2$ sorption on hydrotalcite having a high Mg/Al molar ratio, ACS Appl. Mater. Interfaces 8 (2016) 5763–5767, https://doi.org/10.1021/acsami.5b12598.

[57] N.D. Hutson, S.A. Speakman, E.A. Payzant, Structural effects on the high temperature adsorption of CO $_2$ on a synthetic hydrotalcite, Chem. Mater. 16 (2004) 4135–4143, https://doi.org/10.1021/cm040060u.

[58] Q. Wang, H.H. Tay, D.J.W. Ng, L. Chen, Y. Liu, J. Chang, Z. Zhong, J. Luo, A. Borgna, The effect of trivalent cations on the performance of Mg-M-CO3 layered double hydroxides for high-temperature CO2 capture, ChemSusChem 3 (2010) 965–973, https://doi.org/10.1002/cssc.201000099.

[59] Q. Wang, H.H. Tay, Z. Guo, L. Chen, Y. Liu, J. Chang, Z. Zhong, J. Luo, A. Borgna, Morphology and composition controllable synthesis of Mg–Al–CO3 hydrotalcites by tuning the synthesis pH and the CO2 capture capacity, Appl. Clay Sci. 55 (2012) 18–26, https://doi.org/10.1016/j.clay.2011.07.024.

[60] J.M. Lee, Y.J. Min, K.B. Lee, S.G. Jeon, J.G. Na, H.J. Ryu, Enhancement of CO $_2$ sorption uptake on hydrotalcite by impregnation with K $_2$ CO $_3$, Langmuir 26 (2010) 18788–18797, https://doi.org/10.1021/la102974s.

[61] T.W. Kim, H. Jeong, Y. Jo, D. Kim, J.H. Park, S.K. Kim, Y.-W. Suh, Advanced heterolytic H2 adsorption of K-added Ru/MgO catalysts for accelerating hydrogen storage into aromatic benzyltoluenes, Journal of Energy Chemistry 71 (2022) 333–343, https://doi.org/10.1016/j.jechem.2022.03.047.

[62] M.K. Ram Reddy, Z.P. Xu, G. Q (Max) Lu, And, J.C. Diniz Da Costa, Influence of water on high-temperature CO $_2$ capture using layered double hydroxide derivatives, Ind. Eng. Chem. Res. 47 (2008) 2630–2635. https://doi.org/10.1021/ie0716060.

[63] J.M. Kolle, M. Fayaz, A. Sayari, Understanding the effect of water on CO $_2$ adsorption, Chem. Rev. 121 (2021) 7280–7345, https://doi.org/10.1021/acs.chemrev.0c00762.

[64] Y. Gao, Z. Zhang, J. Wu, X. Yi, A. Zheng, A. Umar, D. O'Hare, Q. Wang, Comprehensive investigation of CO2 adsorption on Mg–Al–CO3 LDH-derived mixed metal oxides, J. Mater. Chem. A 1 (2013) 12782, https://doi.org/10.1039/c3ta13039h.

[65] J. Fagerlund, J. Highfield, R. Zevenhoven, Kinetics studies on wet and dry gas–solid carbonation of MgO and Mg(OH)2 for CO2 sequestration, RSC Adv. 2 (2012) 10380, https://doi.org/10.1039/c2ra21428h.

[66] S. Walspurger, L. Boels, P.D. Cobden, G.D. Elzinga, W.G. Haije, R.W. Van Den Brink, The crucial role of the K $^+$ –aluminium oxide interaction in K $^+$ -promoted alumina- and hydrotalcite-based materials for CO $_2$ sorption at high temperatures, ChemSusChem 1 (2008) 643–650, https://doi.org/10.1002/cssc.200800085.

[67] A.C. Faria, R. Trujillano, V. Rives, C.V. Miguel, A.E. Rodrigues, L.M. Madeira, Alkali metal (Na, Cs and K) promoted hydrotalcites for high temperature CO2 capture from flue gas in cyclic adsorption processes, Chem. Eng. J. 427 (2022) 131502, https://doi.org/10.1016/j.cej.2021.131502.

[68] Y. Duan, K. Zhang, X.S. Li, D.L. King, B. Li, L. Zhao, Y. Xiao, ab initio thermodynamic study of the CO2 capture properties of M2CO3 (M = Na, K)- and CaCO3-promoted MgO sorbents towards forming double salts, aerosol air, Qual. Res. 14 (2014) 470–479, https://doi.org/10.4209/aaqr.2013.05.0178.

[69] S. Jo, H.D. Son, T.-Y. Kim, J.H. Woo, D.Y. Ryu, J.C. Kim, S.C. Lee, K.L. Gilliard-AbdulAziz, Ru/K2CO3–MgO catalytic sorbent for integrated CO2 capture and methanation at low temperatures, Chem. Eng. J. 469 (2023) 143772, https://doi.org/10.1016/j.cej.2023.143772.

[70] K. Coenen, F. Gallucci, G. Pio, P. Cobden, E. Van Dijk, E. Hensen, M. Van Sint Annaland, On the influence of steam on the CO2 chemisorption capacity of a hydrotalcite-based adsorbent for SEWGS applications, Chemical Engineering Journal 314 (2017) 554–569. https://doi.org/10.1016/j.cej.2016.12.013.

[71] K. Coenen, F. Gallucci, E. Hensen, CO2 and H2O chemisorption mechanism on different potassium-promoted sorbents for SEWGS processes, J. CO2 Util. 25 (2018) 180–193, https://doi.org/10.1016/j.jcou.2018.04.002.

[72] X. Ju, L. Liu, P. Yu, J. Guo, X. Zhang, T. He, G. Wu, P. Chen, Mesoporous Ru/MgO prepared by a deposition-precipitation method as highly active catalyst for producing COx-free hydrogen from ammonia decomposition, Appl Catal B 211 (2017) 167–175, https://doi.org/10.1016/j.apcatb.2017.04.043.

[73] K. Sato, S. Miyahara, Y. Ogura, K. Tsujimaru, Y. Wada, T. Toriyama, T. Yamamoto, S. Matsumura, K. Nagaoka, Surface dynamics for creating highly active Ru sites for ammonia synthesis: accumulation of a low-crystalline, oxygen-deficient nanofraction, ACS Sustainable Chem. Eng. 8 (2020) 2726–2734, https://doi.org/10.1021/acssuschemeng.9b06299.

[74] J. Cha, T. Lee, Y.-J. Lee, H. Jeong, Y.S. Jo, Y. Kim, S.W. Nam, J. Han, K.B. Lee, C. W. Yoon, H. Sohn, Highly monodisperse sub-nanometer and nanometer Ru particles confined in alkali-exchanged zeolite Y for ammonia decomposition, Appl Catal B 283 (2021) 119627, https://doi.org/10.1016/j.apcatb.2020.119627.

[75] M. Dosa, M.J. Marin-Figueredo, E. Sartoretti, C. Novara, F. Giorgis, S. Bensaid, D. Fino, N. Russo, M. Piumetti, Cerium-copper oxides synthesized in a multi-inlet vortex reactor as effective nanocatalysts for CO and ethene oxidation reactions, Catalysts 12 (2022) 364, https://doi.org/10.3390/catal12040364.

[76] A. Rizzetto, E. Sartoretti, K. Khoma, M. Armandi, M. Piumetti, S. Bensaid, R. Pirone, The oscillatory behaviour of Cu-ZSM-5 catalysts for N $_2$ O decomposition: investigation of Cu species by complementary techniques, ChemPhysChem 25 (2024) e202400339.

[77] G. Busca, V. Lorenzelli, Infrared spectroscopic identification of species arising from reactive adsorption of carbon oxides on metal oxide surfaces, Mater. Chem. 7 (1982) 89–126, https://doi.org/10.1016/0390-6035(82)90059-1.

[78] J.P. Jolivet, Y. Thomas, B. Taravel, V. Lorenzelli, G. Busca, Infrared spectra of cerium and thorium pentacarbonate complexes, J. Mol. Struct. 79 (1982) 403–408, https://doi.org/10.1016/0022-2860(82)85091-6.

[79] Y. He, D. Mao, Q. Guo, J. Yu, Ru/CeO2 catalyst derived from Ce-based MOF for highly efficient catalytic CO2 methanation integrated with renewable hydrogen, Fuel Process. Technol. 259 (2024) 108101, https://doi.org/10.1016/j.fuproc.2024.108101.

[80] L. Proaño, E. Tello, M.A. Arellano-Trevino, S. Wang, R.J. Farrauto, M. Cobo, In-situ DRIFTS study of two-step CO2 capture and catalytic methanation over Ru,"Na2O"/Al2O3 dual functional material, Appl. Surf. Sci. 479 (2019) 25–30, https://doi.org/10.1016/j.apsusc.2019.01.281.

[81] M. Cavallo, M. Dosa, R. Nakazato, N.G. Porcaro, M. Signorile, M. Quintelier, J. Hadermann, S. Bordiga, N.C. Rosero-Navarro, K. Tadanaga, V. Crocellà, F. Bonino, Insight on Zn-Al LDH as electrocatalyst for CO2 reduction reaction: an in-situ ATR-IR study, J. CO2 Util. 83 (2024) 102804, https://doi.org/10.1016/j.jcou.2024.102804.

[82] F. Yang, X. Liu, C. Xing, Z. Chen, L. Zhao, X. Liu, W. Gao, L. Zhu, H. Liu, W. Zhou, RuCo/ZrO $_2$ tandem catalysts with photothermal confinement effect for enhanced CO $_2$ methanation, Adv. Sci. (2024) 2406828, https://doi.org/10.1002/advs.202406828.

[83] M. León, E. Díaz, S. Bennici, A. Vega, S. Ordóñez, A. Auroux, Adsorption of CO $_2$ on hydrotalcite-derived mixed oxides: sorption mechanisms and consequences for adsorption irreversibility, Ind. Eng. Chem. Res. 49 (2010) 3663–3671, https://doi.org/10.1021/ie902072a.

[84] J.J.C. Struijs, V. Muravev, M.A. Verheijen, E.J.M. Hensen, N. Kosinov, Ceria-supported cobalt catalyst for low-temperature methanation at low partial pressures of CO $_2$, Angew. Chem. Int. Ed. 62 (2023) e202214864.

[85] K. Coenen, F. Gallucci, B. Mezari, E. Hensen, An in-situ IR study on the adsorption of CO2 and H2O on hydrotalcites, J. CO2 Util. 24 (2018) 228–239, https://doi.org/10.1016/j.jcou.2018.01.008.

[86] E. Sartoretti, C. Novara, M.C. Paganini, M. Chiesa, M. Castellino, F. Giorgis, M. Piumetti, S. Bensaid, D. Fino, N. Russo, Investigation of Cu-doped ceria through a combined spectroscopic approach: involvement of different catalytic sites in CO oxidation, Catal. Today 420 (2023) 114037, https://doi.org/10.1016/j.cattod.2023.02.014.

[87] M. Giuliano, M.C. Valsania, P. Ticali, E. Sartoretti, S. Morandi, S. Bensaid, G. Ricchiardi, M. Sgroi, Characterization of the evolution of noble metal particles in a commercial three-way catalyst: correlation between real and simulated ageing, Catalysts 11 (2021) 247, https://doi.org/10.3390/catal11020247.

[88] M. Serrer, M. Stehle, M.L. Schulte, H. Besser, W. Pfleging, E. Saraçi, J. Grunwaldt, Spatially-resolved insights into local activity and structure of Ni-based CO $_2$ methanation catalysts in fixed-bed reactors, ChemCatChem 13 (2021) 3010–3020, https://doi.org/10.1002/cctc.202100490.

[89] J. Zheng, C. Wang, W. Chu, Y. Zhou, K. Köhler, CO $_2$ methanation over supported ru/Al $_2$ O $_3$ catalysts: mechanistic studies by *In situ* infrared spectroscopy, ChemistrySelect 1 (2016) 3197–3203, https://doi.org/10.1002/slct.201600651.

[90] L.-P. Merkouri, J.L. Martín-Espejo, L.F. Bobadilla, J.A. Odriozola, M.S. Duyar, T. R. Reina, Flexible NiRu systems for CO2 methanation: from efficient catalysts to advanced dual-function materials, Nanomaterials 13 (2023) 506, https://doi.org/10.3390/nano13030506.

[91] P. Panagiotopoulou, D.I. Kondarides, X.E. Verykios, Mechanistic study of the selective methanation of CO over Ru/TiO $_2$ catalyst: identification of active surface species and reaction pathways, J. Phys. Chem. C 115 (2011) 1220–1230, https://doi.org/10.1021/jp106538z.

[92] S. Eckle, H.-G. Anfang, R.J. Behm, Reaction intermediates and side products in the methanation of CO and CO $_2$ over supported Ru catalysts in H $_2$ -rich reformate gases, J. Phys. Chem. C 115 (2011) 1361–1367, https://doi.org/10.1021/jp108106t.

[93] B. Peng, Q.-S. Li, Y. Xie, R.B. King, H.F. Schaefer Iii, Unsaturated trinuclear ruthenium carbonyls: large structural differences between analogous carbonyl derivatives of the first, second, and third row transition metals, Dalton Trans. (2008) 6977, https://doi.org/10.1039/b810710f.

[94] S. Navarro-Jaén, A. Szego, L.F. Bobadilla, Ó.H. Laguna, F. Romero-Sarria, M. A. Centeno, J.A. Odriozola, Operando spectroscopic evidence of the induced effect of residual species in the reaction intermediates during CO $_2$ hydrogenation over ruthenium nanoparticles, ChemCatChem 11 (2019) 2063–2068, https://doi.org/10.1002/cctc.201900101.

[95] K. Föttinger, R. Schlögl, G. Rupprechter, The mechanism of carbonate formation on Pd–Al $_2$ O $_3$ catalysts, Chem. Commun. (2008) 320–322, https://doi.org/10.1039/B713161E.

[96] C. Vogt, E. Groeneveld, G. Kamsma, M. Nachtegaal, L. Lu, C.J. Kiely, P.H. Berben, F. Meirer, B.M. Weckhuysen, Unravelling structure sensitivity in CO2 hydrogenation over nickel, Nat Catal 1 (2018) 127–134, https://doi.org/10.1038/s41929-017-0016-y.

[97] J. Lee, J. Otomo, Low-temperature activated direct air capture methanation using K-β″ alumina, Ind. Eng. Chem. Res. 62 (2023) 12096–12108, https://doi.org/10.1021/acs.iecr.3c00828.

[98] E. García-Bordejé, A. Dongil, J. Conesa, A. Guerrero-Ruiz, I. Rodríguez-Ramos, Promotion of Ru or Ni on alumina catalysts with a basic metal for CO2 hydrogenation: effect of the type of metal (Na, K, Ba), Nanomaterials 12 (2022) 1052, https://doi.org/10.3390/nano12071052.

[99] R. Büchel, A. Baiker, S.E. Pratsinis, Effect of Ba and K addition and controlled spatial deposition of Rh in Rh/Al2O3 catalysts for CO2 hydrogenation, Appl. Catal. A 477 (2014) 93–101, https://doi.org/10.1016/j.apcata.2014.03.010.

[100] J. Iloy, Effect of operating temperature, pressure and potassium loading on the performance of silica-supported cobalt catalyst in CO2 hydrogenation to hydrocarbon fuel, Catalysts 9 (2019) 807, https://doi.org/10.3390/catal9100807.

[101] S. Cimino, F. Boccia, L. Lisi, Effect of alkali promoters (Li, Na, K) on the performance of Ru/Al2O3 catalysts for CO2 capture and hydrogenation to methane, J. CO2 Util. 37 (2020) 195–203, https://doi.org/10.1016/j.jcou.2019.12.010.

[102] M.S. Duyar, S. Wang, M.A. Arellano-Treviño, R.J. Farrauto, Co,, 2 utilization with a novel dual function material (DFM) for capture and catalytic conversion to synthetic natural gas: an update, J. CO2 Util. 15 (2016) 65–71, https://doi.org/10.1016/j.jcou.2016.05.003.

[103] A. Tsuneto, A. Kudo, N. Saito, T. Sakata, Hydrogenation of solid state carbonates, Chem. Lett. 21 (1992) 831–834, https://doi.org/10.1246/cl.1992.831.

[104] L. Hu, A. Urakawa, Continuous CO2 capture and reduction in one process: CO2 methanation over unpromoted and promoted Ni/ZrO2, J. CO2 Util. 25 (2018) 323–329, https://doi.org/10.1016/j.jcou.2018.03.013.

[105] M.S. Duyar, M.A.A. Treviño, R.J. Farrauto, Dual function materials for CO 2 capture and conversion using renewable H 2, Appl Catal B 168–169 (2015) 370–376, https://doi.org/10.1016/j.apcatb.2014.12.025.

[106] M.A. Arellano-Treviño, N. Kanani, C.W. Jeong-Potter, R.J. Farrauto, Bimetallic catalysts for CO2 capture and hydrogenation at simulated flue gas conditions, Chem. Eng. J. 375 (2019) 121953, https://doi.org/10.1016/j.cej.2019.121953.

[107] C. Jeong-Potter, A. Porta, R. Matarrese, C.G. Visconti, L. Lietti, R. Farrauto, Aging study of low Ru loading dual function materials (DFM) for combined power plant effluent CO2 capture and methanation, Appl. Catal. B 310 (2022) 121294, https://doi.org/10.1016/j.apcatb.2022.121294.